

THE STAR FORMATION RATE AND GAS SURFACE DENSITY RELATION IN THE MILKY WAY: IMPLICATIONS FOR EXTRAGALACTIC STUDIES

AMANDA HEIDERMAN¹, NEAL J. EVANS II¹, LORI E. ALLEN², TRACY HUARD³, MARK HEYER⁴
Accepted by the Astrophysical Journal

ABSTRACT

We investigate the relation between star formation rate (SFR) and gas surface densities in Galactic star forming regions using a sample of young stellar objects (YSOs) and massive dense clumps. Our YSO sample consists of objects located in 20 large molecular clouds from the *Spitzer* cores to disks (c2d) and Gould’s Belt (GB) surveys. These data allow us to probe the regime of low-mass star formation essentially invisible to tracers of high-mass star formation used to establish extragalactic SFR-gas relations. We estimate the gas surface density (Σ_{gas}) from extinction (A_V) maps and YSO SFR surface densities (Σ_{SFR}) from the number of YSOs, assuming a mean mass and lifetime. We also divide the clouds into evenly spaced contour levels of A_V , counting only Class I and Flat SED YSOs, which have not yet migrated from their birthplace. For a sample of massive star forming clumps, we derive SFRs from the total infrared luminosity and use HCN gas maps to estimate gas surface densities. We find that c2d and GB clouds lie above the extragalactic SFR-gas relations (e.g., Kennicutt–Schmidt Law) by factors up to 17. Cloud regions with high Σ_{gas} lie above extragalactic relations up to a factor of 54 and overlap with high-mass star forming regions. We use ¹²CO and ¹³CO gas maps of the Perseus and Ophiuchus clouds from the COMPLETE survey to estimate gas surface densities and compare to measurements from A_V maps. We find that ¹³CO, with the standard conversions to total gas, underestimates the A_V -based mass by factors of ~ 4 –5. ¹²CO may underestimate the total gas mass at $\Sigma_{\text{gas}} \gtrsim 200 M_{\odot} \text{ pc}^{-2}$ by $\gtrsim 30\%$; however, this small difference in mass estimates does not explain the large discrepancy between Galactic and extragalactic relations. We find evidence for a threshold of star formation (Σ_{th}) at $129 \pm 14 M_{\odot} \text{ pc}^{-2}$. At $\Sigma_{\text{gas}} > \Sigma_{\text{th}}$, the Galactic SFR-gas relation is linear. A possible reason for the difference between Galactic and extragalactic relations is that much of Σ_{gas} is below Σ_{th} in extragalactic studies, which detect all the CO-emitting gas. If the Kennicutt–Schmidt relation ($\Sigma_{\text{SFR}} \propto \Sigma_{\text{gas}}^{1.4}$) and a linear relation between dense gas and star formation is assumed, the fraction of dense star forming gas (f_{dense}) increases as $\sim \Sigma_{\text{gas}}^{0.4}$. When Σ_{gas} reaches $\sim 300 \Sigma_{\text{th}}$, the fraction of dense gas is ~ 1 , creating a maximal starburst.

Subject headings: stars: formation — infrared: stars — ISM: dust — ISM: clouds — galaxies: ISM

1. INTRODUCTION

Understanding how physical processes in the interstellar medium (ISM) control star formation is an important prerequisite to understanding galaxy evolution. A robust measurement of the relation between the star formation rate surface density (Σ_{SFR}) and the surface density of cold gas (Σ_{gas}) is of vital importance for input into theoretical models of galaxy evolution.

The idea that there should be a relation between the density of star formation and gas density was first proposed by Schmidt (1959). Schmidt investigated this relation, now known as the “Schmidt law”, assuming that it should be in the form of a power law and suggested that the density of star formation was proportional to gas density squared. Kennicutt (1998b) measured the global or disk-averaged Schmidt law in a sample of spiral and starburst galaxies using the projected star formation and gas surface densities (Σ_{gas}) in the form:

$$\Sigma_{\text{SFR}} \propto \Sigma_{\text{gas}}^N, \quad (1)$$

where N is the power law index. The global SFR and

Σ_{gas} measurements for the sample of galaxies in Kennicutt (1998b) were fitted to a power law with $N = 1.4$, which is known as in the “Kennicutt–Schmidt law” :

$$\Sigma_{\text{SFR}} = (2.5 \pm 0.7) \times 10^{-4} \left(\frac{\Sigma_{\text{gas}}}{1 M_{\odot} \text{ pc}^{-2}} \right)^{1.4 \pm 0.15} (M_{\odot} \text{ yr}^{-1} \text{ kpc}^{-2}). \quad (2)$$

Since it is only an assumption that there is *only one relation* that regulates how gas is forming stars, we refrain from calling this a “law” and instead refer to it as a SFR–gas relation, or as the Kennicutt–Schmidt relation when referring to equation 2 specifically. Several authors (Larson 1992; Elmegreen 1994; Wong & Blitz 2002; Krumholz & Tan 2007) argue that there is a simple explanation for the Kennicutt–Schmidt relation: if the SFR is proportional to the gas mass divided by the time it takes to convert the gas into stars and if we take this timescale to be the free-fall time, then $t_{\text{ff}} \propto \rho_{\text{gas}}^{-0.5}$ and $\dot{\rho}_{\text{SFR}} \propto \rho_{\text{gas}}^{1.5}$. Taking the scale height to be constant, $\rho \propto \Sigma$, and this in turn gives the Kennicutt–Schmidt relation (to the extent that $1.4 \pm 0.15 = 1.5$). A variety of observational meth-

¹ Department of Astronomy, University of Texas at Austin, 1 University Station C1400, Austin, TX 78712–0259, USA; alh@astro.as.utexas.edu, nje@astro.as.utexas.edu

² National Optical Astronomy Observatory, 950 North Cherry Avenue, Tucson, AZ 85719, USA; lallen@noao.edu

³ Department of Astronomy, University of Maryland, College Park, MD 20742, USA; thuard@astro.umd.edu

⁴ Department of Astronomy, University of Massachusetts, Amherst, MA 01003–9305, USA; heyer@astro.umass.edu

ods have been used to investigate this relation in different types of galaxies and on different scales.

There have been many observational studies of SFR–gas relations on either global scales (Kennicutt 1989, 1998b) or using either radial (Martin & Kennicutt 2001; Wong & Blitz 2002; Boissier et al. 2003; Heyer et al. 2004; Komugi et al. 2005; Schuster et al. 2007) or point-by-point measurements (Kuno et al. 1995; Zhang et al. 2001) that find values of N ranging from 1–2. Recently, there have been studies that measure star formation and gas content of galaxies on spatially resolved scales of ~ 0.2 –2 kpc. These studies have found power law indices of $N \approx 0.8 - 1.6$ (Kennicutt et al. 2007; Thilker et al. 2007; Bigiel et al. 2008; Braun et al. 2009; Blanc et al. 2009; Verley et al. 2010). The study by Bigiel et al. (2008) used a sample of 18 nearby galaxies to derive a spatially resolved relation on ~ 750 pc scales. They found a linear relation between Σ_{SFR} and the molecular gas surface density over a range of 3–50 $M_{\odot} \text{pc}^{-2}$:

$$\Sigma_{\text{SFR}} = 10^{-2.1 \pm 0.2} \left(\frac{\Sigma_{\text{H}_2}}{10 M_{\odot} \text{pc}^{-2}} \right)^{1.0 \pm 0.2} (M_{\odot} \text{yr}^{-1} \text{kpc}^{-2}). \quad (3)$$

Other spatially resolved studies were based on measurements done in a single galaxy on scales of ~ 100 –500 pc: M51 (Kennicutt et al. 2007; Blanc et al. 2009), NGC 7331 (Thilker et al. 2007), M31 (Braun et al. 2009), and M33 (Verley et al. 2010). Since the global study of Kennicutt (1998b) and spatially resolved study of Bigiel et al. (2008) obtain results for large samples of galaxies, we use these studies as a baseline for comparison to our work. It is evident that sensitivity of N to systematic variations in methodology (e.g., data spatial resolution, SFR tracers, power law fitting method) accounts for some of the differences in the derived star formation power law index, but the underlying physical reasons for the variations in the SFR–gas relations remain an open, challenging question.

Krumholz et al. (2009) revisited the SFR–gas relation, considering the dependence on atomic and molecular components of Σ_{gas} , metallicity, and clumping of the gas. Their analysis produces a SF–gas relation that rises steeply at low Σ_{gas} , where the gas is mostly atomic, is nearly linear in the regime where normal spiral galaxies are found (Kennicutt et al. 2007; Bigiel et al. 2008; Blanc et al. 2009), and increases superlinearly above 85 $M_{\odot} \text{pc}^{-2}$. Measurements made in these studies, however, are limited to hundred parsec scales or more and are not directly comparable to the size of individual molecular clouds or dense clumps where stars form. While these studies have all looked at the extragalactic SFR–gas relation, there has been little work until recently investigating this relation locally in the Milky Way.

Surveys of nearby molecular clouds in the Milky Way using *Spitzer* imaging have provided large statistical samples of young stellar object (YSO) candidates (e.g., Allen et al. 2010, in preparation, Evans et al. (2009), Forbrich et al. (2009), Rebull et al. (2010)). These surveys have allowed us to directly count the number of low-mass stars that are forming and estimate SFRs. These data also allow us to trace the low-mass star formation regime essentially invisible to tracers, such as emission in $\text{H}\alpha$, ultraviolet, far-infrared (FIR), and singly ionized

oxygen, used to establish extragalactic SFR–gas relations. Since these tracers only probe the rate at which massive stars form, a stellar Initial Mass Function (IMF), extrapolating down to low stellar masses, must be assumed to obtain a SFR. Thus, these SFR estimates are very sensitive to the IMF slope and distribution on the low-mass end.

Evans et al. (2009) compared extragalactic observed SFR–gas relations to total molecular cloud measurements from the *Spitzer* c2d survey. They found that Galactic clouds lie above the SFR–gas relations predicted by extragalactic work (Bigiel et al. 2008; Kennicutt 1998b) and lie slightly above the extrapolated relation from a study of massive dense clumps (Wu et al. 2005):

$$\text{SFR} \sim 1.2 \times 10^{-8} \left(\frac{M_{\text{dense}}}{M_{\odot}} \right) (M_{\odot} \text{yr}^{-1}). \quad (4)$$

This result suggests that studying SFR–gas relations in our Galaxy may be useful for interpreting star formation observed in nearby and high- z galaxies. On the high-mass end of the spectrum, a large survey of massive dense clumps by Wu et al. (2010), provides a sample that can be directly compared to extragalactic star formation tracers.

In this paper, we extend the comparison by Evans et al. (2009) by combining the 7 c2d clouds and 13 clouds from the GB survey. Regions of high-mass star formation from a survey of ~ 50 massive dense Galactic clumps from Wu et al. (2010) provide an extension to high-mass star formation regions. The layout of this paper is organized as follows. We discuss low-mass star formation in the c2d and GB clouds and describe how Σ_{gas} is derived from extinction maps and estimate SFR surface densities (Σ_{SFR}) by YSO counts in Sections 2.1 and 2.2, respectively. In Section 2.3, we separate clouds into evenly spaced contour intervals of Σ_{gas} , measuring the Σ_{SFR} and Σ_{gas} in these intervals. Section 3 discusses the differences between Galactic and extragalactic gas and SFR surface density relations. A_V and CO measurements of Σ_{gas} are compared in Section 3.1. We investigate whether massive star forming regions behave differently from low-mass star forming regions in Section 3.2. The effects of averaging over whole galaxies (kpc scales), including both star forming gas and diffuse molecular gas, on the SFR–gas relation measured in extragalactic studies are discussed in Section 3.3. Finally, we summarize our results in Section 4.

2. LOW-MASS STAR FORMING REGIONS FROM *Spitzer* C2D AND GOULD’S BELT SURVEYS

The cores to disks (c2d) Legacy project included 5 large clouds: Serpens (Ser), Perseus (Per), Chamaeleon II (Cha II), Ophiuchus (Oph), and Lupus (Lup) (Evans et al. 2009). Because the Lup ‘cloud’ is really composed of several separate clouds, we divide them in this study by name: Lup I, III, and IV, and obtain a total of 7 clouds. The Gould’s Belt (GB) Legacy project (Allen et al. 2010, in preparation) includes 13 large clouds: IC 5146E and IC 5146NW (Harvey et al. 2008), Corona Australis (CrA), Scorpius (Sco), Auriga (Aur), Auriga North (AurN), Serpens-Aquila (Ser-Aqu), Musca (Mus), Cepheus (Cep) (Kirk et al. 2009), Cha I and III, and Lup V and VI. These 20 clouds span a large range of masses, areas, and number of YSOs (see Table 1). The term “large”

was used in the c2d study to distinguish them from the sample of small clouds and cores that were biased toward regions known to have dense gas (Evans et al. 2003). The “large” clouds are thus suitable for statistical analyses, such as those presented here, but they are actually small compared to the Orion cloud or many clouds in the inner Galaxy.

2.1. Estimating Σ_{gas} from Extinction Maps

We derive cloud masses ($M_{\text{gas,cloud}}$) and mean surface densities ($\Sigma_{\text{gas,cloud}}$) from the extinction maps, which were produced from a combination of 2MASS and *Spitzer* data, ranging from $1.25\mu\text{m}$ to $24\mu\text{m}$. In this wavelength range, the spectral energy distributions (SEDs) of sources classified as stars provide measurements of the visual extinction (A_V) along lines of sight through the clouds (Evans et al. 2007; Huard et al. 2010). Line-of-sight extinctions were determined by fitting the SEDs, adopting the Weingartner & Draine (2001) extinction law with $R_V = A_V/E(B - V) = 5.5$. Extinction maps were constructed by convolving these line-of-sight measures with uniformly spaced Gaussian beams. The c2d team observed “off-cloud fields” for four of the molecular clouds: Chamaeleon, Perseus, Ophiuchus, and Lupus. The line-of-sight extinction measurements from these off-cloud fields suggested A_V calibration offsets of 1–2 magnitudes; therefore, in constructing the maps for these four clouds, Evans et al. (2007) subtracted these calibration offsets. Since no off-cloud field had been observed for Serpens, they used a weighted mean of the A_V calibration offsets to correct the calibration of their Serpens extinction maps. No off-cloud fields were observed for the GB survey. Further analysis of the fitting of the line-of-sight extinctions demonstrates that the inferred calibration offsets strongly depend on which wavebands had detections (Huard et al. 2010). For example, sources with only near-infrared (2MASS) detections may suggest no calibration offset, while sources with only mid-infrared (*Spitzer*) detections show greater calibration offsets, perhaps as high as 2–3 magnitudes. This finding suggests that the Weingartner & Draine (2001) extinction law does not accurately characterize the reddening through the full range $1.25\text{--}24\mu\text{m}$ spectral range. For if it did, the inferred A_V calibration offsets should be independent of the detected wavebands. For this reason, the extinction maps delivered by the GB survey make use of the catalogued line-of-sight extinctions with no correction for potential calibration offsets, and, for consistency, they suggest that the previously adopted A_V calibration “offsets” of 1–2 magnitudes be added to the c2d extinction maps (Huard et al. 2010). After revising accordingly the extinctions in the clouds mapped by c2d, we find that the gas masses, and thus the cloud surface densities, are $\sim 20\text{--}30\%$ greater than those previously published by Evans et al. (2009). The extinction maps used in this study probe to higher A_V (up to 40 mag) than some previous studies (e.g., Pineda et al. (2008); Lombardi et al. (2008, 2010)) due to the inclusion of both 2MASS and mid-IR *Spitzer* data.

In order to compute the $M_{\text{gas,cloud}}$, we chose extinction maps with $270''$ beams for all clouds. We base this choice on the best resolution map available for Ophiuchus,

which is limited in resolution due to a large extended region of high extinction with relatively few background stars detected. $M_{\text{gas,cloud}}$ and $\Sigma_{\text{gas,cloud}}$ were calculated by summing up extinction map measurements and converting to the column density using the relation $N_{\text{H}}/A_V = (1.086C_{\text{ext}}(V))^{-1} = 1.37 \times 10^{21} \text{ cm}^{-2} \text{ mag}^{-1}$ (Draine 2003) for a Weingartner & Draine (2001) $R_V = 5.5$ extinction law, where $C_{\text{ext}}(V) = 6.715 \times 10^{-22} \text{ cm}^2/\text{H}$ from the on-line tables⁵, using equation 5 and 6, respectively. The uncertainties in $M_{\text{gas,cloud}}$ are computed from maps of extinction uncertainty, which account for the statistical photometric uncertainties, but not systematic uncertainties in using the extinction law calibration.

We compute $M_{\text{gas,cloud}}$ by summing up all pixels ($\sum A_V$) above $A_V = 2$ in all clouds except for Serpens and Ophiuchus which are covered by the c2d survey completely down to $A_V = 6$ and 3, respectively. $M_{\text{gas,cloud}}$ is then:

$$M_{\text{gas,cloud}} = \mu m_{\text{H}} (1.086 C_{\text{ext}}(V))^{-1} \times \sum A_V \times A_{\text{pixel}} \\ \approx 1.58 \times 10^{-36} \times \sum \left(\frac{A_V}{\text{mag}} \right) \times \left(\frac{A_{\text{pixel}}}{\text{cm}^2} \right) (M_{\odot}) \quad (5)$$

where the mean molecular weight (μ) is 1.37, the total number of hydrogen atoms is $N(\text{H}) \equiv N(\text{HI}) + 2N(\text{H}_2)$, and we assume a standard molecular cloud composition of 63% hydrogen, 36% helium, and 1% dust, m_{H} is the mass of hydrogen in grams, the area of a pixel in square cm (A_{pixel}) in the extinction map is $(\pi/180/3600)^2 \text{ D}(\text{cm})^2 R''^2$, where R'' is the pixel size in arcseconds, and A_{cloud} is the area of the cloud measured in square pc. We divide $M_{\text{gas,cloud}}$ by the area to obtain $\Sigma_{\text{gas,cloud}}$ for each cloud:

$$\Sigma_{\text{gas,cloud}} = \left(\frac{M_{\text{gas,cloud}}}{M_{\odot}} \right) \times \left(\frac{A_{\text{cloud}}}{\text{pc}^2} \right)^{-1} (M_{\odot} \text{ pc}^{-2}) \quad (6)$$

$$\Sigma_{\text{gas,cloud}} = 15 \left(\frac{A_V}{\text{mag}} \right) (M_{\odot} \text{ pc}^{-2}). \quad (7)$$

Measured cloud properties for c2d and GB clouds within a contour of $A_V > 2$ or A_V completeness limit are shown in Table 1.

2.2. Estimating Star Formation Rates from YSO Counts

We estimate the SFR from the total number of YSOs ($N_{\text{YSO,tot}}$) contained in an area where $A_V > 2$, as described in § 2.1. We assume a mean YSO mass ($\langle M_{\text{YSO}} \rangle$) of $0.5 \pm 0.1 M_{\odot}$, where the mean estimated error in mass is derived from the mass distribution of YSOs in Cha II from Spezzi et al. (2008). The mean YSO mass is consistent with IMF studies by Chabrier (2003); Kroupa (2002); Ninkovic & Trajkovska (2006). We also assume a period for star formation ($t_{\text{Class II}}$) of 2 ± 1 Myr, based on the estimate of the elapsed time between formation and the end of the Class II phase (Evans et al. 2009). This SFR assumes that star formation has been continuous over a period greater than $t_{\text{Class II}}$. All clouds have Class III objects, indicating that star formation has continued for longer than $t_{\text{Class II}}$. The SFR measured in this way could be underestimated or overestimated in any particular cloud, but over an ensemble of 20 clouds, it should be the most reliable SFR indicator available because no extrapolation from the

⁵ Tables available at <http://www.astro.princeton.edu/~draine/dust/dustmix.html>

massive star tail of the IMF is needed. We base our error estimates by choosing the largest error from either the systematic error, combined in quadrature from mean YSO mass and period of star formation, or the Poisson error from YSO number counts.

$$\Sigma_{\text{SFR}} = N_{\text{YSO,tot}} \times \left(\frac{\langle M_{\text{YSO}} \rangle}{M_{\odot}} \right) \times \left(\frac{t_{\text{Class II}}}{\text{Myr}} \right)^{-1} \times \left(\frac{A_{\text{cloud}}}{\text{kpc}^2} \right)^{-1} (M_{\odot} \text{ yr}^{-1} \text{ kpc}^{-2}) \quad (8)$$

Table 1 lists values for clouds within a contour of $A_V > 2$ for all c2d and GB clouds. We show our estimated $\Sigma_{\text{gas,cloud}}$ and Σ_{SFR} for the c2d and GB clouds in Figure 1. $\Sigma_{\text{gas,cloud}}$ ranges from $\sim 50\text{--}140 M_{\odot} \text{ pc}^{-2}$, and Σ_{SFR} ranges from $\sim 0.4\text{--}3.4 M_{\odot} \text{ kpc}^{-2} \text{ yr}^{-1}$. We use these units for convenience in comparing to the extragalactic relations.

We compare the observations to the predicted values for Σ_{SFR} using $\Sigma_{\text{gas,cloud}}$ that we calculate for the c2d and GB clouds. We plot these extragalactic relations in Figure 1 and will include them in all the following SFR–gas relation figures. The solid lines represent the regime where they were fitted to data and the dashed lines are extrapolated relations spanning the range of Σ_{gas} . The blue line is from disk-averaged or global SFR measurements based on H α emission and the total (H I + CO) gas surface densities in a sample of normal spirals and starburst galaxies from Kennicutt (1998b). The red line is from Bigiel et al. (2008), who made sub-kpc resolution measurements in a sample of spiral and dwarf galaxies using SFRs based on a combination of *Spitzer* 24 μm and GALEX UV data and use CO measurements to obtain a relation for H $_2$ gas surface density. Both of these studies trace either obscured (24 μm) or unobscured (H α and UV) massive star formation and are blind to regions of low-mass star formation that we are measuring in this work. We also compare to the theoretical total (H I + CO) gas and SFR relation of Krumholz et al. (2009) (orange solid line). This prediction takes into account three factors: the conversion of atomic to molecular gas, metallicity, and clumping of the gas. For our comparisons, we choose galactic solar metallicity and a clumping factor of 1, which corresponds to clumping on 100 pc scales. We include data points for the Taurus molecular cloud, including YSO counts from Rebull et al. (2010), Σ_{gas} from a 2MASS extinction map (Pineda et al. 2010), and the total ^{13}CO and ^{12}CO gas mass from Goldsmith et al. (2008).

If we take the average $\Sigma_{\text{gas,cloud}}$ defined as the total $M_{\text{gas,cloud}}$ divided by the total area (A_{cloud}) in pc^2 , we would find that the average molecular cloud in this study has a surface density of $91.5 M_{\odot} \text{ pc}^{-2}$ and a Σ_{SFR} of $1.2 M_{\odot} \text{ kpc}^{-2} \text{ yr}^{-1}$. Taking this average $\Sigma_{\text{gas,cloud}}$ and calculating what the extragalactic relations would predict for the average cloud SFR surface density, we would get 0.13, 0.07, and $0.03 M_{\odot} \text{ kpc}^{-2} \text{ yr}^{-1}$ for Kennicutt (1998b), Bigiel et al. (2008), and Krumholz et al. (2009), respectively. The observed values exceed the observed extragalactic Σ_{SFR} predictions by factors of $\sim 9\text{--}17$ and the theoretical prediction by a factor of ~ 40 . While the star formation surface density, Σ_{SFR} of $1.2 M_{\odot} \text{ kpc}^{-2} \text{ yr}^{-1}$, seem high, the clouds fill only a small fraction of the local square kpc. From Table 1, the total SFR is $780.5 M_{\odot} \text{ Myr}^{-1}$.

If we remove the IC5146 clouds, which are more distant than 0.5 kpc, the SFR within 0.5 kpc is $748 M_{\odot} \text{ Myr}^{-1}$ or $7.5 \times 10^{-4} M_{\odot} \text{ yr}^{-1}$. Extrapolated to the Galaxy with a star-forming radius of 10 kpc, this would amount to $0.3 M_{\odot} \text{ yr}^{-1}$, less than the rate estimated for the entire galaxy of 0.68 to $1.45 M_{\odot} \text{ yr}^{-1}$ (Robitaille & Whitney 2010). This local, low-mass star formation mode thus could account for a substantial, but not dominant, amount of star formation in our Galaxy.

2.3. Estimating Σ_{gas} and Σ_{SFR} for the Youngest YSOs as a Function of A_V

The last section gave us estimates over the whole molecular cloud including all YSOs in each cloud. Early work surveying large areas of clouds (e.g., Lada (1992)) suggested that star formation is concentrated in regions within molecular clouds in regions of high densities ($n \sim 10^4 \text{ cm}^{-3}$). The c2d and GB studies of many whole clouds have clearly established that star formation is not spread uniformly over clouds, but is concentrated in regions at high extinction. Furthermore, the youngest YSOs and dense cores (Enoch et al. 2007) are the most highly concentrated at high A_V (Evans et al. 2009, Bressert et al. 2010, submitted). Older YSOs can leave their original formation region or even disperse the gas and dust. Taking the average velocity dispersion of a core to be 1 km s^{-1} , a 2 Myr old YSO could travel $\sim 2 \text{ pc}$, roughly the average radius of a cloud in this study. We therefore apply a conservative approach and only estimate the SFRs using the youngest Class I or Flat SED YSOs (see Greene et al. (1994) for the definition of classes) that have not yet migrated from their birth place. To classify YSOs as Class I or Flat SED, we use the extinction corrected spectral index from Evans et al. (2009) for the c2d clouds and the uncorrected spectral index for the GB clouds (Table 1). These two classes of YSOs have timescales of 0.55 ± 0.28 and $0.36 \pm 0.18 \text{ Myr}$, respectively (Allen et al. 2010, in preparation).

In order to measure Σ_{SFR} and Σ_{gas} for the youngest YSOs, we divide the clouds into equally spaced contour levels of A_V or $\Sigma_{\text{gas,con}}$ and measure the SFR, mass (M_{con}), and area (A_{con}) enclosed in that contour level. The contour intervals start from the extinction map completeness limits (§ 2.1) and are spaced such that they are wider than our map beam size of $270''$ as shown in Figure 2. We compute the gas surface density ($\Sigma_{\text{gas,con}}$) in the same way as in equation 6, but this time using only the mass ($M_{\text{gas,con}}$) and area (A_{con}) enclosed in the A_V contour region.

$$\Sigma_{\text{gas,con}} = \left(\frac{M_{\text{gas,con}}}{M_{\odot}} \right) \times \left(\frac{A_{\text{con}}}{\text{pc}^2} \right)^{-1} (M_{\odot} \text{ pc}^{-2}). \quad (9)$$

If there are no YSOs found in the contour region, we compute an upper limit to the SFR by assuming that there is one YSO in that region. The upper limits are denoted by the asterisks in Table 2. We estimate the uncertainties in the both the SFR and Σ_{SFR} by choosing the largest error: either the systematic or Poisson error from YSO counts.

2.3.1. MISidentified YSOs from SED FITS (MISFITS)

The c2d and GB surveys have classified YSOs based on the SED slope from a fit to photometry between $2\mu\text{m}$ and $24\mu\text{m}$ (Evans et al. 2009; Allen et al. 2010, in preparation). However, we find that some of the Class I and Flat SED YSOs are not clustered and lie farther from the extinction peaks than expected for their age. Most of these suspicious objects are found, on average, to lie at $A_V \sim 6$ magnitude. If these Class I and Flat SED objects are true young YSOs, they are more likely to be centrally concentrated toward the densest regions in a cloud (Lada 1992). Class I and Flat SED YSOs should be associated with a dense, centrally concentrated, envelope of gas. We therefore performed a follow up survey of these suspicious objects for a subset of c2d and GB clouds using the Caltech Submillimeter Observatory (CSO). Our work was motivated by a study performed by van Kempen et al. (2009), who mapped $\text{HCO}^+ J=4-3$ using the James Clerk Maxwell Telescope and found that 6 previously classified Class I YSOs in Ophiuchus had no detections down to 0.1 K.

With high effective and critical densities, $n \sim 10^4$ and $\sim 10^6 \text{ cm}^{-3}$ (Evans 1999), the $\text{HCO}^+ J=3-2$ transition provides a good tracer of the dense gas contained in protostellar envelopes. We observed Class I and Flat SED YSOs at the CSO from the Aur, Cep, IC5146, Lup, Oph, Per, Sco, Ser, and Ser-Aqu molecular clouds using the $\text{HCO}^+ J=3-2$ (267.557620 GHz) line transition as a dense stage I gas tracer to test if they are truly embedded YSOs. A survey of all observable c2d and GB clouds with detailed results will be published in a later paper.

Observations were made during June and December of 2009 and July 2010 with an atmospheric optical depth (τ_{225}) ranging from 0.05–0.2. We observed each source using position switching for an average of 120 seconds on and off source. If a source was detected, we integrated until we reach a signal-to-noise of $\geq 2\sigma$ (most sources have $\geq 3\sigma$ detections). Using an average main beam efficiency (η) of 0.80 and 0.61 for December 2009 and July 2010 observing runs, respectively, we compute the main beam temperatures and integrated intensities of detected sources. The results are shown in Table 3.

For this paper, we observed a total of 98 suspicious sources, 45 Flat SED and 53 Class I sources. We find that 74% (73/98) of the observed sources are not detected in $\text{HCO}^+ J=3-2$. Out of the 42 Flat SED sources, we detect only 3, but we detect 42% (22/53) of the Class I sources. The YSO MISFITS are a small fraction of the total number (3146) of YSOs or Class I plus Flat sources (681) in the c2d and GB studies, but they could bias the statistics upward at low gas surface densities. The undetected MISFITS may be background galaxies or later stage YSOs, and we will explore this in more detail in a later paper. Figure 2 shows the distribution of Class I (red filled circles), Flat SED YSOs (yellow filled circles) and non-detected MISFITS, indicated by the open stars on the Per cloud A_V map. MISFITS that we do not detect in $\text{HCO}^+ J=3-2$ are removed from the sample when we measure $\Sigma_{\text{gas,con}}$ and Σ_{SFR} in A_V contours (Section 2.4).

2.4. Results: The Youngest YSOs as a Function of Σ_{gas}

After removing the MISFITS from our Class I and Flat SED YSO sample, we show the number, $M_{\text{gas,con}}$, $\Sigma_{\text{gas,con}}$, SFRs, and Σ_{SFR} in Table 2 for all contour levels in each

cloud or separate cloud component (see Section 2). In Figure 3, we show the $\Sigma_{\text{gas,con}}$ and Σ_{SFR} densities for both Class I and Flat SED sources (green and magenta stars) and upper limits for each class (green and magenta inverted triangles) that we measured in contour regions described in § 2.3, with extragalactic observational relations over-plotted. A wider range in both Σ_{gas} ($\sim 45\text{--}560 M_\odot \text{ pc}^{-2}$), and Σ_{SFR} ($\sim 0.03\text{--}95 M_\odot \text{ kpc}^{-2} \text{ yr}^{-1}$) are found for contour regions compared to the total cloud measurements. We note that the points for Sco and Cep (Kirk et al. 2009) clouds are obtained by co-adding the separate cloud regions using the same contour intervals. Since these points sample regions with non-uniform A_V , they only provide an estimate of Σ_{SFR} and Σ_{gas} . These points lie at $\Sigma_{\text{SFR}} < 6 M_\odot \text{ kpc}^{-2} \text{ yr}^{-1}$ and high $\Sigma_{\text{gas}} > 330 M_\odot \text{ pc}^{-2}$.

We compare our YSO contour results to extragalactic relations and find that most points lie well above the extragalactic relations. Excluding upper limits, the mean values of Σ_{SFR} and $\Sigma_{\text{gas,con}}$ are of $9.7 M_\odot \text{ kpc}^{-2} \text{ yr}^{-1}$ and $225 M_\odot \text{ pc}^{-2}$, respectively. Evaluated at this mean gas surface density, the extragalactic relations under-predict Σ_{SFR} by factors of $\sim 21\text{--}54$. The mean YSO contour lies above the Krumholz et al. (2009) extragalactic SFR–gas relation prediction by ~ 2 orders of magnitude. We explore the differences between the Galactic and extragalactic SFR–gas relations in Section 3.

3. WHY ARE GALACTIC SFR–GAS RELATIONS DIFFERENT FROM EXTRAGALACTIC RELATIONS?

The differences between our findings on Galactic scales and the extragalactic relations, both on global or disk-averaged scales (Kennicutt 1998b) and scales of hundreds of pc (Kennicutt et al. 2007; Thilker et al. 2007; Bigiel et al. 2008; Blanc et al. 2009; Braun et al. 2009; Verley et al. 2010), might be explained in the following ways. Firstly, using ^{12}CO to measure the H_2 in galaxies might give systematically different Σ_{gas} than do A_V measurements (Section 3.1). Secondly, the local c2d and GB clouds are forming low-mass stars; since extragalactic SFR tracers respond only to massive stars, the two star forming regimes might behave differently. In Section 3.2, we will investigate whether massive star forming regions agree with the extragalactic SFR–gas relations and if they vary from low-mass star forming regions. Finally, averaging over whole galaxies on scales of hundreds of pc includes both gas contained in the parts of molecular clouds that are forming stars and diffuse molecular gas that is not forming stars (Section 3.3). A local example of this is a study of the Taurus molecular cloud; Goldsmith et al. (2008), found a large amount of diffuse ^{12}CO at lower gas densities where no young stars are forming. Extragalactic studies averaging over hundreds of pc scales would include this gas, causing an increase in the amount of CO flux that is being counted as star forming gas.

3.1. The use of CO versus A_V to determine Σ_{gas}

Since extinction maps are direct probes of Σ_{gas} , they provide the best measure of the total gas and are optimal for use in determining the Σ_{gas} of molecular clouds. However, A_V maps are not easily obtainable in extragalactic studies, which instead employ CO maps, particularly

$^{12}\text{CO } J=1-0$, to determine Σ_{gas} of molecular hydrogen. Since the molecular hydrogen (H_2) rotational transitions require high temperatures not found in the bulk of molecular clouds, other tracers of dense gas are used to estimate the amount of H_2 . The next most abundant molecule with easily observable excitation properties in a molecular cloud is $^{12}\text{CO } J=1-0$. In this study, we want to explore how well CO traces A_V as a function of M_{gas} or Σ_{gas} . We can directly test this in two galactic clouds, Perseus and Ophiuchus, which both have $^{12}\text{CO } J=1-0$ and $^{13}\text{CO } J=1-0$ maps from the Five College Radio Astronomy Observatory (FCRAO) COordinated Molecular Probe Line Extinction Thermal Emission (COMPLETE) Survey of Star Forming Regions (Ridge et al. 2006).

In order to directly compare the CO maps from the COMPLETE survey to the A_V maps in this study, we interpolate the CO data onto the A_V map grid with a pixel size of $45''$. We integrate the publicly available CO data cubes over the velocity range from $0-15 \text{ km s}^{-1}$ to create moment zero maps of integrated intensity defined as: $I_{\text{CO}}(x, y) \equiv \int T_{\text{mb}}(x, y, z) dV \text{ K km s}^{-1}$, where $T_{\text{mb}} \equiv T_{\text{A}}^*/\eta_{\text{mb}}$ is the main beam brightness temperature defined as the antenna temperature (T_{A}^*) divided by the main beam efficiency (η_{mb}) of 0.45 and 0.49 for $^{12}\text{CO } J=1-0$ and $^{13}\text{CO } J=1-0$, respectively, from Pineda et al. (2008). Corresponding rms noise maps ($\sigma_{T(x,y)}$) were constructed by calculating the standard deviation of intensity values within each spectroscopic channel where no signal is detected. In order to determine the gas surface density of H_2 (Σ_{H_2}), we must first compute the column density of H_2 . The column density of H_2 is estimated from the ^{12}CO map by using a CO-to- H_2 conversion factor (X_{CO}), which is defined as the ratio of H_2 column density to the integrated intensity ($X_{\text{CO}} \equiv N_{\text{H}_2}/I_{\text{CO}}$). Similarly for the ^{13}CO map, the column density is derived from the ^{12}CO and ^{13}CO maps, assuming LTE and an abundance ratio of H_2 -to- ^{13}CO . To compare Σ_{H_2} from ^{12}CO and ^{13}CO to the Σ_{gas} from A_V , we use only regions in the CO maps that have emission lines with positive integrated intensities and line peaks that are greater than 5 times the rms noise. Our masses from extinction measurements used for this comparison are therefore slightly lower than those in Tables 1 and 2 by $\sim 5\%$ (See Tables 4 and 5).

The X_{CO} factor for ^{12}CO has been derived using a variety of methods such as gamma ray emission caused by the collision of cosmic rays with hydrogen (Bloemen et al. 1986), virial mass methods (Solomon et al. 1987; Blitz et al. 2007), maps of dust emission from *IRAS* and assuming a constant dust-to-gas ratio (Frerking et al. 1982), extinction maps from optical star counts (Duvert et al. 1986; Bachiller & Cernicharo 1986; Langer et al. 1989) and 2MASS data (Lombardi et al. 2006; Pineda et al. 2008), and theoretically by the assumption that giant molecular clouds are in gravitational equilibrium (Dickman et al. 1986; Heyer et al. 2001). All these studies find a range of X_{CO} of $0.9-4.8 \times 10^{20} \text{ cm}^{-2} \text{ K}^{-1} \text{ km}^{-1} \text{ s}$, but they were almost all restricted to regions with $A_V < 6 \text{ mag}$. Studies of extragalactic SFR-gas relations chose values close to the average galactic X_{CO} measurements in the literature: $2.0 \times 10^{20} \text{ cm}^{-2} \text{ K}^{-1} \text{ km}^{-1}$ (Bigiel et al. 2008) or $2.8 \times 10^{20} \text{ cm}^{-2} \text{ K}^{-1} \text{ km}^{-1} \text{ s}$ from Bloemen et al. (1986) (Kennicutt

1998b; Kennicutt et al. 2007; Blanc et al. 2009). Since the goal of this study is to compare to extragalactic measurements, we choose a X_{CO} of $2.8 \pm 0.7 \times 10^{20} \text{ cm}^{-2} \text{ K}^{-1} \text{ km}^{-1} \text{ s}$ from Bloemen et al. (1986) to be consistent with the study of Kennicutt (1998b).

We compute the column density of H_2 from ^{12}CO measurements using the equation:

$$N_{\text{H}_2(^{12}\text{CO})} = X_{^{12}\text{CO}} \times I_{^{12}\text{CO}} \text{ (cm}^{-2}\text{)}. \quad (10)$$

This can be rewritten in terms of gas surface density:

$$\begin{aligned} \Sigma_{\text{H}_2(^{12}\text{CO})} &= (2m_{\text{H}} \times N_{\text{H}_2(^{12}\text{CO})} \times A_{\text{pixel}}) / A_{\text{cloud}} \\ &\approx 10^{-33} \times m_{\text{H}} \times \left(\frac{N_{\text{H}_2(^{12}\text{CO})}}{\text{cm}^{-2}} \right) \times \left(\frac{A_{\text{pixel}}}{\text{cm}^2} \right) \times \\ &\quad \left(\frac{A_{\text{cloud}}}{\text{pc}^2} \right)^{-1} (M_{\odot} \text{ pc}^{-2}), \end{aligned}$$

where we take the total number of hydrogen atoms is $N(\text{H}) \equiv 2N(\text{H}_2)$. We use this factor of two instead of the mean molecular weight of H_2 ($\mu_{\text{H}_2} = 2.8$, derived from cosmic abundances of 71% hydrogen, 27% helium, and 2% metals, e.g., Kauffmann et al. (2008)) to be consistent with the extragalactic studies of Kennicutt (1998b) and Bigiel et al. (2008). This factor of 2 does not account for helium, which is an additional factor of ~ 1.36 (Hildebrand 1983). The errors in our gas surface density measurements include both the error from the rms intensity maps and the error in the CO-to- H_2 conversion factor from Bloemen et al. (1986).

The top two panels of Figure 4 show the ^{12}CO integrated intensity versus the visual extinction derived from the 2MASS and *Spitzer* data for both Per (left) and Oph (right). We over-plot the conversion factor derived from the gamma ray study of Bloemen et al. (1986) (dashed line). ^{12}CO is seen to correlate with A_V out to $A_V \sim 7-10$, where ^{12}CO starts to saturate and the distribution flattens out to higher A_V . A large difference in the amount of ^{12}CO integrated intensity produced relative to that predicted by $X_{^{12}\text{CO}}$ between the Per and Oph molecular clouds is seen. This may be due to higher opacity at higher A_V in Oph relative to Per. Extinction values around 10–20 mag are found to be essentially invisible to ^{12}CO . This figure demonstrates the non-linear, non-monotonic behavior of CO emission with A_V .

^{12}CO , however, is not the most reliable tracer of star forming gas because of high opacity and varying ^{12}CO -to- H_2 abundance due to photodissociation or depletion on to dust grains. Studies of molecular clouds (Carpenter et al. 1995; Heyer et al. 1996; Goldsmith et al. 2008) show that ^{12}CO contains a significant diffuse component in the low column density regime $A_V < 4$. ^{13}CO emission is a more reliable tracer of dense gas ranging from $1000-7000 \text{ cm}^{-3}$ than ^{12}CO because it is optically thin for most conditions within a cloud and ^{13}CO abundance variations are small for densities $< 5000 \text{ cm}^{-3}$ and temperatures of $> 15 \text{ K}$ (Bachiller & Cernicharo 1986; Duvert et al. 1986; Heyer & Ladd 1995; Caselli et al. 1999).

To estimate the column densities from the $^{13}\text{CO } J=1-0$ integrated intensity maps we assume local thermodynamic equilibrium (LTE), optically thin $^{13}\text{CO } J=1-0$, and that $^{12}\text{CO } J=1-0$ and $^{13}\text{CO } J=1-0$ have equivalent excitation

temperatures. In order to derive column densities, we also determine an optical depth ($\tau_{13\text{CO}}$) and excitation temperature (T_{ex}) from comparison to the $^{12}\text{CO } J=1-0$ line. We can derive this by assuming the $^{12}\text{CO } J=1-0$ is optically thick; as $\tau \rightarrow \infty$,

$$T_{\text{ex}} = \frac{5.5}{\ln\left(1 + \frac{5.5}{T_{\text{peak}, 12\text{CO}} + 0.82}\right)} \text{ (K)}, \quad (11)$$

where $T_{\text{peak}, 12\text{CO}}$ is the $^{12}\text{CO } J=1-0$ peak main beam brightness temperature which we measure on a pixel-by-pixel basis.

The $^{13}\text{CO } J=1-0$ optical depth is then

$$\tau_{13\text{CO}} = -\ln\left(1 - \frac{T_{\text{peak}, 13\text{CO}}}{5.3} \left[\frac{1}{\exp(5.3/T_{\text{ex}}) - 1} - 0.16\right]^{-1}\right), \quad (12)$$

where $T_{\text{peak}, 13\text{CO}}$ is the $^{13}\text{CO } J=1-0$ peak main beam brightness temperature measured in each pixel. We can then use the definition of ^{13}CO optical depth and column density from Rohlfs & Wilson (1996) to estimate the column density of ^{13}CO :

$$N_{13\text{CO}} = 2.6 \times 10^{14} \left(\frac{\tau_{13\text{CO}}}{1 - \exp(-\tau_{13\text{CO}})} \right) \times \left(\frac{I_{13\text{CO}}}{1 - \exp(-5.3/T_{\text{ex}})} \right) \text{ (cm}^{-2}\text{)}. \quad (13)$$

Certain regions near A_V peaks in the clouds are optically thick and are affected by ^{12}CO self absorption. In these regions, we cannot accurately determine T_{ex} and therefore $\tau_{13\text{CO}}$. This problem affects $\sim 10\%$ of the pixels in Oph ($A_V > 30$ mag) and $\sim 5\%$ of the pixels in Per ($A_V > 20$ mag). Since most of the mass lies at low A_V , we mask out the pixels that have ^{13}CO self absorption and do not include them in determining the ^{13}CO column density and mass estimate discussed below.

For comparison with extragalactic work, where clouds are not resolved, we derive ^{13}CO column densities by using average spectra to determine T_{ex} and $\tau_{13\text{CO}}$ using a $T_{\text{peak}, 12\text{CO}}$ of 3 and 5.3 K and a $T_{\text{peak}, 13\text{CO}}$ of 0.7 and 1.5 K for Per and Oph, respectively. Comparing the two methods, we find that using peak temperatures from average spectra or a constant T_{ex} and $\tau_{13\text{CO}}$ will result in higher $N_{13\text{CO}}$ by a factor of ~ 2 at $A_V < 10$ over the pixel-by-pixel measurements.

In order to convert the $N_{13\text{CO}}$ column density into H_2 column density, we use a H_2 -to- ^{13}CO abundance ratio. The $\text{H}_2/^{13}\text{CO}$ abundance ratio for the Per cloud was determined by Pineda et al. (2008), who found a value of $3.98 \pm 0.07 \times 10^5$ for $A_V < 5$ mag. Dividing the cloud into separate regions, they found an average abundance ratio of 3.8×10^5 . Other values found in the literature range from 3.5 – 6.7×10^5 , with an average value of $\sim 4 \times 10^5$ using both extinction maps (Pineda et al. 2008) and star counts (Bachiller & Cernicharo 1986; Duvert et al. 1986; Langer et al. 1989). We adopt the average $\text{H}_2/^{13}\text{CO}$ ratio from the literature of $(4 \pm 0.4) \times 10^5$ to convert ^{13}CO to H_2 column densities using the relation:

$$N_{\text{H}_2(13\text{CO})} = (4 \pm 0.4) \times 10^5 N_{13\text{CO}} \text{ (cm}^{-2}\text{)} \quad (14)$$

or in terms of surface densities:

$$\Sigma_{\text{H}_2(13\text{CO})} = (2m_{\text{H}} \times N_{\text{H}_2(13\text{CO})} \times A_{\text{pixel}}) / A_{\text{cloud}} \\ \approx 10^{-33} \times m_{\text{H}} \times \left(\frac{N_{\text{H}_2(13\text{CO})}}{\text{cm}^{-2}} \right) \times \left(\frac{A_{\text{pixel}}}{\text{cm}^2} \right) \times \left(\frac{A_{\text{cloud}}}{\text{pc}^2} \right)^{-1} \text{ (M}_{\odot} \text{ pc}^{-2}\text{)},$$

where we choose a factor of two instead of the mean molecular weight in order to consistently compare to ^{12}CO . We show the ^{13}CO integrated intensity versus the visual extinction derived from the 2MASS and *Spitzer* data for both Per (left) and Oph (right) in the bottom two panels of Figure 4. The average $\text{H}_2/^{13}\text{CO}$ ratio is shown by the dashed line. A turnover in ^{13}CO is seen at $A_V \sim 7$ (Per) and ~ 10 (Oph) that is likely due to an increase in optical depth. The amount of ^{13}CO in Per follows the average abundance ratio out to $A_V \sim 5$, but in Oph, the ^{13}CO integrated intensity is underproduced.

To test how well CO traces A_V as a function of M_{gas} or Σ_{gas} , we measure Σ_{gas} densities in our A_V maps and Σ_{H_2} in the CO maps in the overlapping area where there is a positive CO integrated intensity over 5 times the rms noise. In Figure 5, we plot the ratio of Σ_{H_2} and Σ_{gas} from A_V , which are effectively mass ratios, since the area measured is the same. The cyan squares and circles are points for the c2d and GB clouds ($\Sigma_{\text{H}_2(12\text{CO, cloud})}$, $\Sigma_{\text{H}_2(13\text{CO, cloud})}$) and the filled green and yellow squares and circles are measurements in contours of A_V using the same method as in Section 2.3 ($\Sigma_{\text{H}_2(12\text{CO, con})}$, $\Sigma_{\text{H}_2(13\text{CO, con})}$) for Oph and Per, respectively (Tables 4 and 5). A measurement for the Taurus cloud using both ^{12}CO and ^{13}CO above $A_V = 2$ from (Goldsmith et al. 2008) is also shown (cyan triangle). If CO traces the mass we find using extinction maps, we would expect the ratio of CO/ A_V mass to be of order unity as shown by the solid black line in Figure 5. For ^{12}CO , we find the total cloud measurement for Per to have Σ_{H_2} of $\sim 1.6\Sigma_{\text{gas}}$ at $\Sigma_{\text{gas}} \lesssim 100 \text{ M}_{\odot} \text{ pc}^{-2}$, but the ratio is close to unity within the errors. We find that ^{12}CO traces A_V relatively well in the Oph cloud out to $\sim 200 \text{ M}_{\odot} \text{ pc}^{-2}$. At $\Sigma_{\text{gas}} \gtrsim 200 \text{ M}_{\odot} \text{ pc}^{-2}$, ^{12}CO underestimates the A_V mass in both Per and Oph by $\sim 30\%$, on average.

Since ^{13}CO should trace denser gas (Duvert et al. 1986; Bachiller & Cernicharo 1986), we also explore how it traces A_V as a function of Σ_{gas} . We plot this on Figure 5 for the total clouds (cyan points) and contour measurements (green points). We find a constant value of ^{13}CO versus the surface density of extinction, but find that it underestimates Σ_{gas} by a factor of ~ 4 – 5 and lies below measurements of ^{12}CO by a factor of ~ 5 , on average. The difference we find between ^{13}CO and H_2 measured by A_V , could be due to the LTE method we used to compute ^{13}CO masses or the assumption that there is a constant abundance of CO relative to H_2 . Heyer et al. (2009) explored the properties of galactic molecular clouds using ^{13}CO emission and found that the assumption of equivalent excitation temperatures for both ^{12}CO and ^{13}CO in the LTE method may underestimate the true column density of ^{13}CO in subthermally excited regions. As the ^{13}CO density increases, the $J=1-0$ transition becomes thermalized, and the column density estimates are more accurate. Also, both Heyer et al. (2009) and Goldsmith et al. (2008)

found that if ^{13}CO -to- H_2 abundance variations in LTE-derived cloud masses are not considered, they would underestimate the true column densities by factors of 2–3. Since we only include ^{13}CO emission greater than 5 times the rms noise, we are likely measuring gas that is thermalized with little abundance variation. Assuming a constant abundance ratio will therefore not account for the difference between A_V and ^{13}CO masses. ^{13}CO , might therefore be a more consistent tracer of Σ_{gas} , but it may underestimate the mass by factors of ~ 4 –5, which can be corrected for.

Variations in the CO-to- H_2 conversion factor may impact the slope of the SFR–gas relations as measured by extragalactic studies. Since we are resolving molecular clouds, we cannot place constraints on gas densities lower than $\sim 50 M_\odot \text{ pc}^{-2}$, typical of spiral galaxies (Bigiel et al. 2008). However if we consider the effects of using CO as a tracer of the total gas density, it underestimates the mass measured from A_V by $\gtrsim 30\%$ for $\Sigma_{\text{gas}} \gtrsim 200 M_\odot \text{ pc}^{-2}$. This would effectively shift the extragalactic observed points to the right above $200 M_\odot \text{ pc}^{-2}$. This shift would flatten the slope slightly in the fitted Kennicutt (1998b) relation. These small factors, however do not explain the large discrepancy between the extragalactic relations and the much higher SFR in the local clouds, seen both in the whole molecular clouds and looking at the youngest YSOs as a function of Σ_{gas} .

3.2. Do High-mass and Low-mass Star Forming Regions Behave Differently?

By studying nearby molecular clouds, we can obtain the most accurate measurement of Σ_{gas} and Σ_{SFR} , but it is regions of *massive* star formation that form the basis for extragalactic studies. Massive star forming regions are the only readily visible regions forming stars at large distances and thus are the only probes of star formation in distant regions in the Milky Way and external galaxies. We can measure Σ_{SFR} and Σ_{gas} in individual massive star forming regions to see if there is better agreement with extragalactic SFR–gas relations.

To investigate where individual regions of massive star formation fall on the SFR–gas relation, we use data from the molecular line survey of dense gas tracers in > 50 massive dense ($\langle n \rangle \sim 10^6 \text{ cm}^{-3}$, e.g. Plume et al. (1997)) clumps from Wu et al. (2010). The Wu et al. (2010) survey measured clump sizes, virial masses, and dense gas surface densities using HCN $J=1-0$ as a tracer (Σ_{HCN}) at FWHM of the peak intensity. These are the sites of formation of clusters and massive stars. The most popular tracers of massive star formation include the ultraviolet, $\text{H}\alpha$, FIR, and singly ionized oxygen; however, due to high extinction toward and in these regions, we can use only the total IR luminosity to measure the SFR in these massive clumps.

Since HCN $J=1-0$ gas has been shown to be tightly correlated with the total IR luminosity in clumps as long as $L_{\text{IR}} > 10^{4.5} L_\odot$ (Wu et al. 2005), as well as in both normal spiral and starburst galaxies (Gao & Solomon 2004a,b), we can use it to compare gas and star formation from the total IR luminosity in both the Milky Way and external galaxies.

Σ_{HCN} is calculated using the mass contained within the

FWHM size (R_{HCN}) of the HCN gas, following the methods used in Shirley et al. (2003):

$$\Sigma_{\text{HCN}} = \pi^{-1} \times \left(\frac{M_{\text{vir}}}{M_\odot} \right) \left(\frac{R_{\text{HCN}}}{\text{pc}} \right)^{-2} (M_\odot \text{ pc}^{-2}), \quad (15)$$

where M_{vir} is the virial mass enclosed in the source size at FWHM intensity. Uncertainties in the Σ_{HCN} are computed by adding in quadrature the errors in the FWHM size and the mass as discussed in Wu et al. (2010).

We compute the SFR for massive dense clumps following extragalactic methods using the total infrared (IR) luminosity (L_{IR} ; 8–1000 μm) derived from the 4 IRAS bands. We assume the conversion $\text{SFR}_{\text{IR}} (M_\odot \text{ yr}^{-1}) \approx 2 \times 10^{-10} L_{\text{IR}} (L_\odot)$ from Kennicutt (1998a). $\Sigma_{\text{SFR}_{\text{IR}}}$ are computed using the FWHM source sizes:

$$\Sigma_{\text{SFR}_{\text{IR}}} = \pi^{-1} \times \left(\frac{\text{SFR}_{\text{IR}}}{M_\odot \text{ yr}^{-1}} \right) \left(\frac{R_{\text{HCN}}}{\text{kpc}} \right)^{-2} (M_\odot \text{ yr}^{-1} \text{ kpc}^{-2}). \quad (16)$$

The uncertainties in the $\Sigma_{\text{SFR}_{\text{IR}}}$ density only include the error in FWHM size and a 30% error in SFR calibrations using the IR. In fact, the uncertainties are larger. The SFR calibration assumes that the observed far-IR emission is re-radiated by dust heated by O, B, and A stars (Kennicutt 1998a). For low SFR, heating by older stars of dust unrelated to star formation can contaminate the SFR signal, causing an overestimate of the SFR. This is not a problem for the regions of massive star formation in our Galaxy, where the heating is certainly due to the recent star formation. A bigger issue for the Galactic regions is that the full L_{IR} seen in the extragalactic studies is not reached unless the individual region forms enough stars to fully sample the IMF and is old enough that the stars have reached their full luminosity. These conditions may not be met during the time span of an individual massive clump (Krumholz & Thompson 2007; Urban et al. 2010). In particular, Urban et al. (2010) have calculated the ratio of luminosity to SFR in a simulation of a cluster forming clump. They find that L/SFR increases rapidly with time, but lies a factor of 3–10 below the relation in Kennicutt (1998a) when their simulations end at times of 0.7 to 1.4 Myr. Therefore, we may expect both large variations and a tendency to underestimate the SFR in individual regions. Unfortunately, despite these issues, L_{IR} remains the best measure of SFR available to us at present in these regions. While it would be suspect to apply a correction factor based on the Urban et al. simulation, increasing the SFR of the regions of massive star formation by 0.5–1 order of magnitude would bring them into better agreement with the highest surface density points from the nearby clouds.

For the sample of ~ 50 massive dense clumps, 42 sources have corresponding IR measurements. The resulting gas surface densities and Σ_{SFR} for the sample of massive dense clumps are shown in Figure 6 and Table 6. The relation between SFR and dense gas mass, $M_{\text{dense}}(\text{H}_2)$, for galactic clumps can be derived from $\langle L_{\text{IR}}/L_{\text{HCN}(1-0)} \rangle = 911 \pm 227 (\text{K km s}^{-1} \text{ pc}^2)^{-1}$, and $\langle M_{\text{dense}}(\text{H}_2)/L_{\text{HCN}(1-0)} \rangle = 11 \pm 2 M_\odot (\text{K km s}^{-1} \text{ pc}^2)^{-1}$ from Wu et al. (2005). These relations can be combined with the IR SFR conversion from above to obtain a relation for $\Sigma_{\text{SFR}_{\text{IR}}}$ and Σ_{HCN} :

$$\Sigma_{\text{SFR}_{\text{IR}}} \sim 1.66 \times 10^{-2} \left(\frac{\Sigma_{\text{HCN}(1-0)}}{1 M_{\odot} \text{ pc}^{-2}} \right) (M_{\odot} \text{ yr}^{-1} \text{ kpc}^{-2}). \quad (17)$$

This equation is equivalent to that shown in Wu et al. (2005), which is the fit to both massive clumps and galaxies.

Wu et al. (2005) found a decline in the linear $L - L'_{\text{HCN}(1-0)}$ correlation at $L_{\text{IR}} < 10^{4.5} L_{\odot}$, where the clump is not massive or old enough to sample the IMF. Since the majority of the points with $L_{\text{IR}} < 10^{4.5} L_{\odot}$ in Figure 6 lie off this relation, we include only massive dense clumps with $L_{\text{IR}} > 10^{4.5} L_{\odot}$. The resulting number of HCN $J=1-0$ sources is 25 (Table 6). The HCN $J=1-0$ clumps are found to range from $\sim 10^2 - 4.5 \times 10^3 M_{\odot} \text{ pc}^{-2}$ in Σ_{HCN} and from $2 - 130 M_{\odot} \text{ kpc}^{-2} \text{ yr}^{-1}$ in $\Sigma_{\text{SFR}_{\text{IR}}}$. These Σ_{gas} and $\Sigma_{\text{SFR}_{\text{IR}}}$ values are similar to those of circumnuclear starburst galaxies from Kennicutt (1998b), which range from $\sim 10^2 - 6 \times 10^4 M_{\odot} \text{ pc}^{-2}$ and $0.1 - 9.5 \times 10^2 M_{\odot} \text{ kpc}^{-2} \text{ yr}^{-1}$ (see Figure 9). The average HCN $J=1-0$ clump has $\Sigma_{\text{HCN}(1-0)}$ of $(1.3 \pm 0.2) \times 10^3 M_{\odot} \text{ pc}^{-2}$ and $\Sigma_{\text{SFR}_{\text{IR}}}$ of $28 \pm 6 M_{\odot} \text{ kpc}^{-2} \text{ yr}^{-1}$.

We also compare the relation we find for the massive dense clumps to known extragalactic relations in Figure 7. In this figure we compare to the H_2 gas surface density relation from Bigiel et al. (2008) and the total ($\text{H I} + \text{H}_2$) gas surface density relation from Kennicutt (1998b). We find that most of the points for the HCN $J=1-0$ line lie above both the Bigiel et al. (2008) and Kennicutt (1998b) extragalactic relations with the average clump lying a factor of $\sim 5 - 20$ above the Kennicutt (1998b) and Bigiel et al. (2008) relations, respectively.

In Figure 8 we plot the ratio of $\Sigma_{\text{SFR}}/\Sigma_{\text{gas}}$ versus Σ_{gas} for c2d and GB clouds, YSOs, and massive clumps. We find a steep decline in Σ_{SFR} and $\Sigma_{\text{SFR}}/\Sigma_{\text{gas}}$ at around $\sim 100 - 200 M_{\odot} \text{ pc}^{-2}$. We identify this steep change in Σ_{SFR} over $\sim 100 - 200 M_{\odot} \text{ pc}^{-2}$ as a star forming threshold (Σ_{th}) between regions actively forming stars and those that are forming few or no low-mass stars.

In Figure 9 we show points for the massive dense clumps, c2d and GB clouds, the youngest YSOs, and both the Wu et al. (2005) and extragalactic relations. We also show the range of gas surface densities for spiral and circumnuclear starburst galaxies from the sample of Kennicutt (1998b). $\Sigma_{\text{gas,con}}$ for Class I and Flat SED YSOs lie intermediate between the regions where spiral galaxies and starburst galaxies are found on the Kennicutt (1998b) relation. At $\Sigma_{\text{gas}} > \Sigma_{\text{th}}$, the youngest Class I and Flat SED YSOs overlap with the massive clumps (Figure 9). Therefore, high-mass and low-mass star forming regions behave similarly in the $\Sigma_{\text{SFR}} - \Sigma_{\text{gas}}$ plane. The difference between extragalactic relations and c2d and GB clouds is not caused by the lack of massive stars in the local clouds. Also, the overlap with the massive clumps in Figure 9 suggests that L_{IR} provides a reasonable SFR indicator, as long as it exceeds $10^{4.5} L_{\odot}$, though an upward correction would produce better agreement.

A steep increase and possible leveling off in Σ_{SFR} at a threshold $\Sigma_{\text{th}} \sim 100 - 200 M_{\odot} \text{ pc}^{-2}$ is seen in both Figures 8 and 9. We further constrain this steep increase and the possibility of Σ_{SFR} flattening at $\Sigma_{\text{gas}} > \Sigma_{\text{th}}$, by approximating it as broken power law with a steep rise that

levels off in Section 3.2.1.

3.2.1. Star Formation Threshold

In order to determine a robust estimate of Σ_{th} , we fit the data using two models: a single power law ($y = Nx + A$, where $y = \log_{10} \Sigma_{\text{SFR}}$; $x = \log_{10} \Sigma_{\text{gas}}$ and a broken power law ($y_1 = N_1x + A_1$; $y_2 = N_2x + A_2$). We first fit Class I and Flat SED YSO points ($\Sigma_{\text{SFR,con}}, \Sigma_{\text{gas,con}}$) and massive clumps ($\Sigma_{\text{SFR}_{\text{IR}}}, \Sigma_{\text{HCN}(1-0)}$) to a single power law. We do not include upper limits for YSOs or points for Sco and Cep clouds, which are co-added separate cloud regions and only provide a rough estimate of Σ_{SFR} and Σ_{gas} . The single power law fit yields $N = 1.57 \pm 0.09$ and $A = -3.0 \pm 0.2$, and a reduced chi-square (χ_r^2) of 3.7 (84 dof). We fit the data for both YSOs and massive clumps to a broken power law for the range of $\Sigma_{\text{gas}} = 50 - 250 M_{\odot} \text{ pc}^{-2}$. We minimize the total χ^2 for the two segments of the broken power law using a simplex routine, which yields best fit parameters: $N_1 = 4.58 \pm 0.5$, $A_1 = -9.18 \pm 0.9$, $N_2 = 1.12 \pm 0.07$, $A_2 = -1.89 \pm 0.2$ with a χ_r^2 of 3.04 (82 dof). We attribute the large χ_r^2 to the scatter and large errors in the data, but since the χ_r^2 is $\sim 18\%$ lower for the broken power law compared to the single power law, we take it to be the best fit model. Equating the broken power law fits ($y_1 = y_2$), we obtain a power law break at $\Sigma_{\text{th}} = 129.2 M_{\odot} \text{ pc}^{-2}$ ($A_V = 8.6$) with a statistical 1-sigma deviation in χ^2 of $\pm 14 M_{\odot} \text{ pc}^{-2}$ giving a range in Σ_{th} of $\sim 115 - 143 M_{\odot} \text{ pc}^{-2}$. Figure 10 shows the broken power law fit (cyan and magenta lines), Σ_{th} , and the 1-sigma statistical range of Σ_{th} (dashed black vertical line and grey shaded region, respectively). The slope of the broken power law changes from a steep relation at $\Sigma_{\text{gas}} < \Sigma_{\text{th}}$ (slope of ~ 4.6) to linear relation (slope of ~ 1.1) at $\Sigma_{\text{gas}} > \Sigma_{\text{th}}$. We note however, that variations in cloud distances will change this threshold slightly. One example is for Ser, which has a recent distance estimate by Dzib et al. (2010) of 415 pc and another estimate by Straizys et al. (1996) of 260 pc (used in this paper). If we use the larger distance of 415 pc, this would change our star formation threshold slightly to $126 \pm 12 M_{\odot} \text{ pc}^{-2}$ ($A_V = 8.4$).

This star forming threshold we find is in agreement with the threshold found in a study of local molecular clouds by Lada, Lombardi, & Alves (2010, submitted) at $A_V \sim 7$ or $116 M_{\odot} \text{ pc}^{-2}$. Enoch et al. (2007) also found extinction thresholds for dense cores found in Bolo-cam 1.1mm maps in the Perseus, Serpens, and Ophiuchus clouds of $A_V \sim 8, 15$, and 23, respectively ($\sim 120, 225$, and $350 M_{\odot} \text{ pc}^{-2}$), with a low probability of finding cores below these thresholds. Onishi et al. (1998) surveyed Taurus in C^{18}O and found a star forming column density threshold of $8 \times 10^{21} \text{ cm}^{-2}$, which corresponds to a gas surface density of $128.1 M_{\odot} \text{ pc}^{-2}$ ($A_V = 8.5$). Similarly, both Johnstone et al. (2004) and André et al. (2010) find thresholds of $A_V \sim 10$ ($150 M_{\odot} \text{ pc}^{-2}$).

Mouschovias & Spitzer (1976) proposed the idea of a physical column density threshold corresponding to the central surface density above which the interstellar magnetic field cannot support the gas from self gravitational collapse. This was later modified by McKee (1989) who considered the local ionization states owing to UV radiation. Mouschovias & Spitzer (1976) predicted that when clumps combine to form a large cloud complex, there ex-

ists a natural surface density threshold (Σ_{crit}) for a given magnetic field:

$$\Sigma_{\text{crit}} > \left(\frac{80}{M_{\odot} \text{ pc}^2} \right) \times \left(\frac{B}{30 \mu\text{G}} \right). \quad (18)$$

The total mean strength of the line-of-sight magnetic field (B_{los}) measured in molecular clouds ($n \sim 10^3\text{--}10^4 \text{ cm}^3$) is $\sim 10\text{--}20 \mu\text{G}$ (Crutcher 1999; Troland & Crutcher 2008). Since statistically $B_{\text{los}} \approx \frac{1}{2} B_{\text{tot}}$ (Heiles & Crutcher 2005), the corresponding total magnetic field, B_{tot} , is $\sim 20\text{--}40 \mu\text{G}$. Using equation 18, the corresponding $\Sigma_{\text{crit}} > 50\text{--}110 M_{\odot} \text{ pc}^2$. A similar idea of a threshold at a particular extinction was predicted by McKee (1989) for photoionization-regulated star formation. This model predicts that the rate of star formation is controlled by ambipolar diffusion and therefore depends on the ionization levels in the cloud. Star formation in a “standard” ionization case will occur at $A_V \gtrsim 4\text{--}8$ mag, which translates into a $\Sigma_{\text{crit}} \gtrsim 60\text{--}120 M_{\odot} \text{ pc}^2$. Both of these predictions for a critical density of star formation are similar to $\Sigma_{\text{th}} = 129 \pm 14 M_{\odot} \text{ pc}^2$. We note, however, that both these models are for parts of clouds that are in a “quasi-static” or turbulence-supported state. Alternatively, these parts of clouds may never become bound and are transient (Vázquez-Semadeni et al. 2009). In this picture, the threshold would correspond to parts of molecular clouds that become gravitationally bound and form stars.

3.3. Does the Lack of Resolution in Extragalactic Studies Explain the Discrepancy in Σ_{SFR} ?

The third possibility is based on the fact that the extragalactic relations are averaging over large scales which do not resolve the regions where stars are forming. Current “spatially resolved” extragalactic measurements are still limited to scales of $\sim 0.2\text{--}2 \text{ kpc}$ (Kennicutt et al. 2007; Bigiel et al. 2008; Blanc et al. 2009); therefore, we cannot directly measure extragalactic SFRs on scales of galactic star forming regions. In any given spatially resolved extragalactic measurement of Σ_{SFR} and Σ_{gas} , the beam will contain a fraction of diffuse gas that does not trace star formation and a fraction of dense, star forming gas (f_{dense}). As discussed in Section 3.1, the dense gas that is forming stars is not well traced by CO so there will be an excess of non-star forming gas in each beam measurement. A local example of this is a study of the Taurus molecular cloud; Goldsmith et al. (2008) found that 33% of diffuse ^{12}CO is contained in regions not associated with ^{13}CO , which is a more reliable tracer of dense, star forming gas (Section 3.1). Even in the regions with $A_V > 2$ studied by the c2d and GB projects, star formation is highly concentrated to regions of high extinction (e.g., Figure 2). Extragalactic studies averaging over hundreds of pc scales would include this diffuse gas, causing an increase in the amount of CO flux that is being counted as star forming gas. In order to better understand approximately how much gas is forming stars at present, a measurement of the fraction of gas that contains YSOs over a larger area on kpc scales in the Galaxy is needed.

Lada & Lada (2003) proposed the idea that clusters of stars which form in clumps located in giant molecular clouds are the fundamental building blocks of galaxies. The rate at which these stellar clusters form is set by the

mechanisms that enable these clumps to condense out of their low density parent cloud. A similar idea was explored by Wu et al. (2005), who proposed that there is a basic unit of clustered star formation with the following typical properties: $L_{\text{IR}} > 10^5 L_{\odot}$, $R_{\text{dense}} \sim 0.5 \text{ pc}$, and $M_{\text{vir}} \sim 300\text{--}1000 M_{\odot}$. As more of these basic units are contained in a galaxy, the SFR increases linearly. This linear correlation between SFR_{IR} and the mass of dense gas (M_{dense}) from HCN $J=1\text{--}0$ was seen in a sample of both spiral and luminous or ultra-luminous IR galaxies (LIRGS and ULIRGS) (Gao & Solomon 2004b), and Wu et al. (2005) showed that the same relation fit the Galactic massive dense clumps. It is therefore the dense gas tracers, such as HCN, that directly probe the volume of gas from which stars form in dense clumps and produce the star formation in external galaxies.

If a linear relation between dense gas and the SFR is assumed at all Σ_{gas} and Σ_{SFR} densities, how can we explain the non-linear behavior of the Kennicutt–Schmidt SFR–gas relation? Let us suppose that the underlying star formation relation is what we actually observe in regions forming massive stars: a threshold around $129 M_{\odot} \text{ pc}^{-2}$ and a roughly linear relation between dense gas and star formation above that threshold:

$$\Sigma_{\text{SFR}} \propto \Sigma_{\text{dense}}. \quad (19)$$

Let us also assume, the Kennicutt–Schmidt relation for the gas surface density averaged over large scales ($\langle \Sigma_{\text{gas}} \rangle$):

$$\Sigma_{\text{SFR}} \propto \langle \Sigma_{\text{gas}} \rangle^{1.4}. \quad (20)$$

Then, the fraction of gas above the threshold (f_{dense}) would have to scale with mean surface density of all gas:

$$\begin{aligned} f_{\text{dense}} &= \Sigma_{\text{dense}} / \langle \Sigma_{\text{gas}} \rangle \\ &\propto \Sigma_{\text{SFR}} / \langle \Sigma_{\text{gas}} \rangle \\ &\propto \langle \Sigma_{\text{gas}} \rangle^{0.4}. \end{aligned} \quad (21)$$

Near the Σ_{th} of $\sim 129 M_{\odot} \text{ pc}^{-2}$, the average Σ_{SFR} measured on small scales is about $\sim 3 M_{\odot} \text{ yr}^{-1} \text{ kpc}^{-2}$ (taking the average between Class I and Flat SED sources) and f_{dense} is about $1/40$. When $\langle \Sigma_{\text{gas}} \rangle \sim 300 \Sigma_{\text{th}}$, $f_{\text{dense}} \sim 1$. At this point, all the gas is dense enough to form stars and star formation is most efficient, creating a maximal starburst. This is also where the dense gas (Wu et al. 2005) and CO (Kennicutt 1998a) relations cross (see Figure 8). Above $\sim 300 \Sigma_{\text{th}}$, the only way to increase star formation efficiency is to make it more efficient even in the dense gas. This is possible because even in dense gas, the star formation rate per free-fall time is less than unity (Zuckerman & Evans 1974; Krumholz & Tan 2007).

Is there local evidence for a preponderance of gas below the threshold? Complete maps of CO for the local 0.5 kpc are not readily available, but we can measure the mass below and the mass above the threshold of $A_V = 8$ for the 16 clouds with Spitzer coverage down to $A_V = 2$. The ratio of total mass lying below the threshold to the total mass above the threshold is 4.6. The massive star forming region, Orion, also has a similar ratio of 5.1 for the mass below over the mass above $A_V = 8$ (M. Heyer, unpublished data). A few clouds have been mapped to still lower levels and a factor of two more mass is found in Taurus, for example Goldsmith et al. (2008). Alternatively, if we assume Orion to contain the largest reservoir

of molecular material within 0.5 kpc, we can derive the ratio of mass from ^{12}CO and A_V maps to get 6.4 (M. Heyer, unpublished data). Taken together, these factors make it plausible that there is 10 times more molecular mass than mass above the threshold. Furthermore, most of the gas within 0.5 kpc is atomic. If that is included, the predictions of the extragalactic Kennicutt–Schmidt relation for total gas agree reasonably with the local star formation rate surface density (see Evans (2008) and references therein).

Finally, if the underlying star formation law in the dense gas is linear, then the arguments invoking the density dependence of the free-fall time to get a power of 1.5 (see Section 1) are specious. In fact, the idea of a single free-fall time for a molecular cloud with an enormous range of densities is highly dubious in the first place.

4. SUMMARY

We investigate the relation between star formation rate (SFR) and gas surface densities in a sample of young stellar objects (YSOs) and massive dense clumps. Our YSO sample consists of objects located in 20 large molecular clouds from the *Spitzer* cores to disks (c2d) and Gould’s Belt (GB) surveys. We estimate the Σ_{gas} in the c2d and GB clouds from A_V maps and Σ_{SFR} from the number of YSOs, assuming a mean mass and star formation timescale for each source. We also divide the clouds into evenly spaced contour levels of A_V . In each contour interval, we measure the $\Sigma_{\text{gas,con}}$ and estimate the Σ_{SFR} by counting only Class I and Flat SED YSOs which have not yet migrated from their birthplace. We use ^{12}CO and ^{13}CO gas maps of the Perseus and Ophiuchus clouds from the COMPLETE survey to estimate Σ_{H_2} densities and compare to measurements from A_V maps. We also compare the c2d and GB low-mass star forming regions to a sample of massive star forming clumps from Wu et al. (2010). We derive SFRs from the total IR luminosity and use HCN gas maps to estimate SFR surface densities ($\Sigma_{\text{SFR,IR}}$) and gas surface densities (Σ_{HCN}) for the massive clumps. Our results are as follows:

- The c2d and GB clouds lie above the extragalactic SFR–gas relations (e.g., Kennicutt–Schmidt Law) by factors of 9–17. We compare the total cloud points to the theoretical prediction of Krumholz et al. (2009) for galactic metallicity and a clumping factor of 1, corresponding to scales of 100 pc, and find the clouds to lie above this prediction by a factor of ~ 40 .
- We perform a follow up survey of suspicious YSOs (MISFITS) at the CSO using the $\text{HCO}^+ J=3-2$ line transition as a dense gas tracer. We choose the youngest YSOs (Class I and Flat SED) that have not yet had time to migrate from their birthplace. These sources are spatially positioned at low extinction levels, most are not clustered, and most lie outside the A_V peaks. In this paper, we present results for a total of 98 sources, including 45 Flat SED and 53 Class I YSOs (detailed results from the full survey will be published in a later paper). We find that 74% or 73 out of the 98 MISFITS observed to date are not detected in HCO^+ which

indicates that they do not have a dense envelope of gas, and could be either later class YSOs or background galaxies. These are a small fraction of the total number of YSOs in the sample, but they could bias the statistics upward at low Σ_{gas} .

- We divide the c2d and GB clouds into contours using evenly spaced intervals of A_V (Section 2.2). We count only the youngest YSOs, removing any Class I or Flat SED YSOs (MISFITS) that are not detected in HCO^+ (Sections 2.3.1 and 2.4). We find that the observed extragalactic relations (Kennicutt 1998b; Bigiel et al. 2008) under-predict the average Σ_{SFR} of $\sim 9.7 M_\odot \text{ yr}^{-1} \text{ kpc}^{-2}$ by factors of ~ 21 –54 and that our data lie above the theoretical relation (Krumholz et al. 2009) by ~ 2 orders of magnitude.
- We compare Σ_{gas} calculated from A_V maps to Σ_{H_2} estimated from ^{12}CO in Section 3.1. We find that the mass estimated from ^{12}CO may underestimate the Σ_{gas} at $\Sigma_{\text{gas}} \gtrsim 200 M_\odot \text{ pc}^{-2}$ by $>30\%$ (Figure 8). If the Σ_{H_2} from ^{12}CO underestimates the H_2 mass at $\Sigma_{\text{gas}} \gtrsim 200 M_\odot \text{ pc}^{-2}$, then this would effectively shift the extragalactic observed data to the right above this threshold, flattening the slope in the Kennicutt (1998b) relation. However, this small change is not enough to account for the discrepancy between Galactic and extragalactic measurements.
- We also compare Σ_{H_2} from ^{13}CO maps to Σ_{gas} from A_V maps. If ^{13}CO traces the mass we find using extinction maps, we would expect the ratio of $^{13}\text{CO}/A_V$ mass to be of order unity. However, we find the mass estimated from ^{13}CO to be lower than the A_V mass by factors of ~ 4 –5 (Section 3.1).
- We find a steep decrease in $\Sigma_{\text{SFR}}/\Sigma_{\text{gas}}$ (Figure 8) and denote this as a star formation threshold (Σ_{th}). In order to determine Σ_{th} , we fit a single power law and broken power law models to data for Class I and Flat SED YSOs and massive clumps. We find the best fit to the SFR–gas relation between YSOs and clumps to be a broken power law (Section 3.2.1) with a break $\Sigma_{\text{th}} = 129 \pm 14 M_\odot \text{ pc}^{-2}$. We find a steep relation at $\Sigma_{\text{gas}} < \Sigma_{\text{th}}$ (slope of ~ 4.6) and a linear relation at $\Sigma_{\text{gas}} > \Sigma_{\text{th}}$ with a slope of ~ 1.1 (Section 3.2.1).
- Since the c2d and GB clouds are forming low-mass stars, and extragalactic studies are only able to use tracers that measure the light coming from massive stars, the two star forming regimes might behave differently, accounting for the large difference we measure. However, we find that both high and low-mass star forming regions in the Galaxy follow roughly the same linear relation above Σ_{th} (Section 3.2).
- A contributing factor to the difference seen between Milky Way clouds and extragalactic measurements both on disk-averaged and spatially resolved scales is that extragalactic measurements average over large scales. These measurements include both

star forming gas and gas that is not dense enough to form stars.

- Assuming the Kennicutt-Schmidt relation and that the fundamental correlation between Σ_{SFR} and the dense gas (Σ_{dense}) is linear, then the fraction of dense star-forming gas is proportional to $\langle \Sigma_{\text{gas}} \rangle^{0.4}$. When $\langle \Sigma_{\text{gas}} \rangle$ reaches $\sim 300 \Sigma_{\text{th}}$, the fraction of dense gas is ~ 1 , creating a maximal starburst.

The authors thank Mark Krumholz, Charles Lada, Guillermo Blanc, Miranda Dunham, Amanda Bayless, and Jaime Pineda for informative discussions. A.H. and N.J.E. acknowledge support for this work, part of the Spitzer Legacy Science Program, provided by NASA through contract 1288664 issued by the Jet Propulsion Laboratory, California Institute of Technology, under NASA contract 1407 and from NSF Grant AST-0607793 to the University of Texas at Austin, and the State of Texas. L.A. and T.H. are supported by the Gould's Belt Spitzer Legacy grant 1298236. M.H. is supported by NSF grant AST-0832222.

REFERENCES

- André, P., et al. 2010, *A&A*, 518, L102
 Allen, L. et al., 2010, *ApJ*, in preparation.
 Bachiller, R., & Cernicharo, J. 1986, *A&A*, 166, 283
 Bigiel, F., Leroy, A., Walter, F., Brinks, E., de Blok, W. J. G., Madore, B., & Thornley, M. D. 2008, *AJ*, 136, 2846
 Blanc, G. A., Heiderman, A., Gebhardt, K., Evans, N. J., & Adams, J. 2009, *ApJ*, 704, 842
 Blitz, L., Fukui, Y., Kawamura, A., Leroy, A., Mizuno, N., & Rosolowsky, E. 2007, *Protostars and Planets V*, 81
 Bloemen, J. B. G. M., et al. 1986, *A&A*, 154, 25
 Boissier, S., Prantzos, N., Boselli, A., & Gavazzi, G. 2003, *MNRAS*, 346, 1215
 Braun, R., Thilker, D. A., Walterbos, R. A. M., & Corbelli, E. 2009, *ApJ*, 695, 937
 Bressert, E. et al., 2010, *MNRAS*, submitted.
 Carpenter, J. M., Snell, R. L., & Schloerb, F. P. 1995, *ApJ*, 445, 246
 Caselli, P., Walmsley, C. M., Tafalla, M., Dore, L., & Myers, P. C. 1999, *ApJL*, 523, L165
 Chabrier, G. 2003, *PASP*, 115, 763
 Crutcher, R. M. 1999, *ApJ*, 520, 706
 Dickman, R. L., Snell, R. L., & Schloerb, F. P. 1986, *ApJ*, 309, 326
 Draine, B. T. 2003, *ARAA*, 41, 241
 Duvert, G., Cernicharo, J., & Baudry, A. 1986, *A&A*, 164, 349
 Dzib, S., Loinard, L., Mioduszewski, A. J., Boden, A. F., Rodríguez, L. F., & Torres, R. M. 2010, *ApJ*, 718, 610
 Elmegreen, B. G. 1994, *ApJL*, 425, L73
 Enoch, M. L., Glenn, J., Evans, II, N. J., Sargent, A. I., Young, K. E., & Huard, T. L. 2007, *ApJ*, 666, 982
 Evans, N. J., et al. 2009, *ApJS*, 181, 321
 Evans, II, N. J. 1999, *ARAA*, 37, 311
 Evans, II, N. J. 2008, in *Astronomical Society of the Pacific Conference Series*, Vol. 390, *Pathways Through an Eclectic Universe*, ed. J. H. Knapen, T. J. Mahoney, & A. Vazdekis, 52
 Evans, N. J., et al. 2007, *Final Delivery of Data from the c2d Legacy Project: IRAC and MIPS (Pasadena: SSC)*
 Evans, II, N. J., et al. 2003, *PASP*, 115, 965
 Forbrich, J., Lada, C. J., Muench, A. A., Alves, J., & Lombardi, M. 2009, *ApJ*, 704, 292
 Frerking, M. A., Langer, W. D., & Wilson, R. W. 1982, *ApJ*, 262, 590
 Gao, Y., & Solomon, P. M. 2004a, *ApJS*, 152, 63
 —. 2004b, *ApJ*, 606, 271
 Goldsmith, P. F., Heyer, M., Narayanan, G., Snell, R., Li, D., & Brunt, C. 2008, *ApJ*, 680, 428
 Greene, T. P., Wilking, B. A., Andre, P., Young, E. T., & Lada, C. J. 1994, *ApJ*, 434, 614
 Harvey, P. M., et al. 2008, *ApJ*, 680, 495
 Heiles, C., & Crutcher, R. 2005, in *Lecture Notes in Physics*, Berlin Springer Verlag, Vol. 664, *Cosmic Magnetic Fields*, ed. R. Wielebinski & R. Beck, 137
 Heyer, M., Krawczyk, C., Duval, J., & Jackson, J. M. 2009, *ApJ*, 699, 1092
 Heyer, M. H., Carpenter, J. M., & Ladd, E. F. 1996, *ApJ*, 463, 630
 Heyer, M. H., Carpenter, J. M., & Snell, R. L. 2001, *ApJ*, 551, 852
 Heyer, M. H., Corbelli, E., Schneider, S. E., & Young, J. S. 2004, *ApJ*, 602, 723
 Heyer, M. H., & Ladd, E. F. 1995, *ApJ*, 439, 269
 Hildebrand, R. H. 1983, *QJRAS*, 24, 267
 Huard, T., et al. 2020, *Final Delivery of Data from the Gould's Belt Legacy Project: IRAC and MIPS (Pasadena: SSC)*, in preparation.
 Johnstone, D., Di Francesco, J., & Kirk, H. 2004, *ApJL*, 611, L45
 Kauffmann, J., Bertoldi, F., Bourke, T. L., Evans, II, N. J., & Lee, C. W. 2008, *A&A*, 487, 993
 Kennicutt, Jr., R. C. 1989, *ApJ*, 344, 685
 —. 1998a, *ARAA*, 36, 189
 —. 1998b, *ApJ*, 498, 541
 Kennicutt, Jr., R. C., et al. 2007, *ApJ*, 671, 333
 Kirk, J. M., et al. 2009, *ApJS*, 185, 198
 Komugi, S., Sofue, Y., Nakanishi, H., Onodera, S., & Egusa, F. 2005, *PASJ*, 57, 733
 Kroupa, P. 2002, *Science*, 295, 82
 Krumholz, M. R., McKee, C. F., & Tumlinson, J. 2009, *ApJ*, 693, 216
 Krumholz, M. R., & Tan, J. C. 2007, *ApJ*, 654, 304
 Krumholz, M. R., & Thompson, T. A. 2007, *ApJ*, 669, 289
 Kuno, N., Nakai, N., Handa, T., & Sofue, Y. 1995, *PASJ*, 47, 745
 Lada, C. J., & Lada, E. A. 2003, *ARAA*, 41, 57
 Lada, E. A. 1992, *ApJL*, 393, L25
 Langer, W. D., Wilson, R. W., Goldsmith, P. F., & Beichman, C. A. 1989, *ApJ*, 337, 355
 Larson, R. 1992, in *Star Formation in Stellar Systems*, ed. G. Tenorio-Tagle, M. Prieto, & F. Sanchez, 125
 Lombardi, M., Alves, J., & Lada, C. J. 2006, *A&A*, 454, 781
 Lombardi, M., Lada, C. J., & Alves, J. 2008, *A&A*, 489, 143
 —. 2010, *A&A*, 512, A67
 Martin, C. L., & Kennicutt, Jr., R. C. 2001, *ApJ*, 555, 301
 McKee, C. F. 1989, *ApJ*, 345, 782
 Mouschovias, T. C., & Spitzer, Jr., L. 1976, *ApJ*, 210, 326
 Ninkovic, S., & Trajkovska, V. 2006, *Serbian Astronomical Journal*, 172, 17
 Onishi, T., Mizuno, A., Kawamura, A., Ogawa, H., & Fukui, Y. 1998, *ApJ*, 502, 296
 Pineda, J. E., Caselli, P., & Goodman, A. A. 2008, *ApJ*, 679, 481
 Pineda, J. L., Goldsmith, P. F., Chapman, N., Snell, R. L., Li, D., Cambresy, L., & Brunt, C. 2010, *ArXiv e-prints*
 Plume, R., Jaffe, D. T., Evans, II, N. J., Martin-Pintado, J., & Gomez-Gonzalez, J. 1997, *ApJ*, 476, 730
 Rebull, L. M., et al. 2010, *ApJS*, 186, 259
 Ridge, N. A., et al. 2006, *AJ*, 131, 2921
 Robitaille, T. P., & Whitney, B. A. 2010, *ApJL*, 710, L11
 Rohlfs, K., & Wilson, T. L. 1996, *Tools of Radio Astronomy (XVI)* (Springer-Verlag Berlin Heidelberg New York)
 Schmidt, M. 1959, *ApJ*, 129, 243
 Schuster, K. F., Kramer, C., Hirschfeld, M., Garcia-Burillo, S., & Mookerjee, B. 2007, *A&A*, 461, 143
 Shirley, Y. L., Evans, II, N. J., Young, K. E., Knez, C., & Jaffe, D. T. 2003, *ApJS*, 149, 375
 Solomon, P. M., Rivolo, A. R., Barrett, J., & Yahil, A. 1987, *ApJ*, 319, 730
 Spezzini, L., et al. 2008, *ApJ*, 680, 1295
 Straizys, V., Cernis, K., & Bartasiute, S. 1996, *Baltic Astronomy*, 5, 125
 Thilker, D. A., et al. 2007, *ApJS*, 173, 572
 Troland, T. H., & Crutcher, R. M. 2008, *ApJ*, 680, 457
 Urban, A., Martel, H., & Evans, N. J. 2010, *ApJ*, 710, 1343
 van Kempen, T. A., van Dishoeck, E. F., Salter, D. M., Hogerheijde, M. R., Jørgensen, J. K., & Boogert, A. C. A. 2009, *A&A*, 498, 167
 Vázquez-Semadeni, E., Gómez, G. C., Jappsen, A., Ballesteros-Paredes, J., & Klessen, R. S. 2009, *ApJ*, 707, 1023
 Verley, S., Corbelli, E., Giovanardi, C., & Hunt, L. K. 2010, *A&A*, 510, A64
 Weingartner, J. C., & Draine, B. T. 2001, *ApJ*, 548, 296
 Wong, T., & Blitz, L. 2002, *ApJ*, 569, 157
 Wu, J., Evans, N. J., Shirley, Y. L., & Knez, C. 2010, *ApJS*, 188, 313
 Wu, J., Evans, II, N. J., Gao, Y., Solomon, P. M., Shirley, Y. L., & Vanden Bout, P. A. 2005, *ApJL*, 635, L173
 Zhang, Q., Fall, S. M., & Whitmore, B. C. 2001, *ApJ*, 561, 727
 Zuckerman, B., & Evans, II, N. J. 1974, *ApJL*, 192, L149

TABLE 1
MEASURED QUANTITIES FOR CLOUDS.

Cloud	$N_{\text{YSOs,tot}}$	$N_{\text{YSOs,I}}$	$N_{\text{YSOs,F}}$	Distance (pc)	Ω (deg ²)	A_{cloud} (pc ²)	$M_{\text{gas,cloud}}$ (M_{\odot})	$\Sigma_{\text{gas,cloud}}$ (M_{\odot} pc ⁻²)	SFR (M_{\odot} Myr ⁻¹)	Σ_{SFR} (M_{\odot} yr ⁻¹ kpc ⁻²)
(1)	(2)	(3)	(4)	(5)	(6)	(7)	(8)	(9)	(10)	(11)
Cha II	24	0	2	178±18	1.0	9.9±2.0	637.4±296.3	64.3±26	6.0±3.2	0.61±0.35
Lup I	13	2	1	150±20	1.3	8.9±2.4	512.5±308.2	57.9±31	3.2±1.8	0.37±0.22
Lup III	68	2	6	200±20	1.3	15.4±3.1	912.1±517.3	59.1±31	17.0±9.2	1.10±0.63
Lup IV	12	1	0	150±20	0.4	2.5±0.7	189.3±95.5	75.1±32	3.0±1.6	1.19±0.72
Oph	290	27	44	125±25	6.2	29.6±11.8	3115.3±1754.3	105.4±41	72.5±39.0	2.45±1.65
Per	385	76	35	250±50	3.8	73.2±29.3	6585.3±3557.1	90.0±32	96.2±51.8	1.32±0.88
Ser	224	31	21	260±10	0.8	17.0±1.3	2336.7±640.2	137.3±36	56.0±30.2	3.29±1.79
AurN	2	1	0	300±30	0.1	2.4±0.5	223.9±51.9	92.8±10	0.5±0.3	0.21±0.12
Aur	171	43	24	300±30	1.8	50.0±10.0	4617.5±1072.7	92.4±10	42.8±23.0	0.86±0.49
Cep	118	30	10	300±30	1.4	38.0±7.6	2610.3±168.5	68.7±17	29.5±15.9	0.78±0.45
Cha III	4	1	0	200±20	2.3	28.0±5.6	1326.0±386.2	47.4±10	1.0±0.5	0.04±0.02
Cha I	89	10	12	200±20	0.8	9.4±1.9	857.3±206.3	91.1±12	22.2±12.0	2.36±1.36
CrA	41	7	3	130±25	0.6	3.0±1.2	279.2±114.0	92.3±12	10.2±5.5	3.39±2.24
IC5146E	93	13	9	950±80	0.2	61.4±10.3	3365.2±872.9	54.8±10	23.2±12.5	0.38±0.21
IC5146NW	38	16	3	950±80	0.3	87.6±14.8	5178.1±1257.3	59.1±10	9.5±5.1	0.11±0.06
Lup VI	45	0	1	150±20	1.0	6.7±1.8	454.9±141.4	67.5±10	11.2±6.1	1.67±1.00
Lup V	43	0	0	150±20	1.7	11.7±3.1	704.7±223.5	60.5±10	10.8±5.8	0.92±0.55
Mus	12	1	0	160±20	0.9	6.8±1.7	335.1±109.1	49.1±10	3.0±1.6	0.44±0.26
Sco	10	2	1	130±15	1.4	7.3±1.7	620.6±17.4	85.2±22	2.5±1.3	0.34±0.20
Ser-Aqu	1440	146	96	260±10	8.7	179.5±13.8	24441.3±3025.2	136.2±13	360.0±193.9	2.01±1.09
Cloud Averages	156.1±71.5	20.5±7.9	13.4±5.2	274.6±53.3	1.8±0.5	32.4±9.6	2965.1±1204.9	79.3±5.8	39.0±17.9	1.2±0.2
Cloud Total	3122.0	409.0	268.0	-	36.0	648.3	59302.7	91.5	780.5	1.2
Data from Literature:										
Taurus ^I	148	-	-	137	44	252	27207	108	37	0.147

Note. — Columns are : (1) Cloud name.; (2) Total number of YSOs at all A_V .; (3) Number of Class I objects at all A_V .; (4) Number of Flat SED objects at all A_V .; (5) Distances to each cloud.; (6) Solid angle.; (7) Area (pc²).; (8) Mass (M_{\odot}).; (9) Surface gas density (M_{\odot} pc⁻²).; (10) Star formation rate (M_{\odot} Myr⁻¹).; (11) Star formation rate density (M_{\odot} yr⁻¹ kpc⁻²).; (I) Total A_V mass from Pineda et al. (2010) and YSO data from Rebull et al. (2010).

TABLE 2
MEASURED QUANTITIES FOR CLOUDS IN A_V CONTOURS

Cloud	$N_{\text{YSOs,I}}$	$N_{\text{YSOs,F}}$	Contour levels ^I	Ω (deg ²)	A_{con} (pc ²)	M_{con} (M_{\odot})	$\Sigma_{\text{gas,con}}$ (M_{\odot} pc ⁻²)	SFR, I (M_{\odot} Myr ⁻¹)	SFR, F (M_{\odot} Myr ⁻¹)	$\Sigma_{\text{SFR,I}}$ (M_{\odot} yr ⁻¹ kpc ⁻²)	$\Sigma_{\text{SFR,F}}$ (M_{\odot} yr ⁻¹ kpc ⁻²)
(1)	(2)	(3)	(4)	(5)	(6)	(7)	(8)	(9)	(10)	(11)	(12)
Cha II	0	0	5.2	0.8	7.78±1.57	416.9±223.1	53.6±26.6	0.9±1.0*	1.4±1.0*	0.1±0.1*	0.2±0.1*
Cha II	0	1	8.2	0.2	1.76±0.36	162.6±58.7	92.3±27.6	0.9±1.0*	1.4±1.0	0.5±0.6*	0.8±0.6
Cha II	0	1	11.8	0.03	0.30±0.06	43.9±12.7	147.0±30.4	0.9±1.0*	1.4±1.0	3.0±3.3*	4.7±3.3
Cha II	1	0	16.0	0.01	0.07±0.01	14.0±3.8	193.9±34.7	0.9±1.0	1.4±1.0*	12.6±13.8	19.2±13.8*
Lup I	1	0	6.0	1.2	8.05±2.15	417.5±273.2	51.9±31.0	0.9±1.0	1.4±1.0*	0.1±0.1	0.2±0.1*
Lup I	0	0	10.0	0.1	0.71±0.19	77.8±31.0	109.3±32.4	0.9±1.0*	1.4±1.0*	1.3±1.4*	2.0±1.4*
Lup I	0	0	16.0	0.01	0.09±0.02	17.2±5.8	184.1±39.0	0.9±1.0*	1.4±1.0*	9.8±10.7*	14.9±10.7*
Lup III	1	2	8.0	1.2	14.89±2.98	815.8±490.4	54.8±31.1	0.9±1.0	2.8±1.5	0.1±0.1	0.2±1.4
Lup III	0	1	14.0	0.03	0.42±0.08	65.0±20.3	153.1±36.6	0.9±1.0*	1.4±1.0	2.1±2.4*	3.3±2.4
Lup III	1	0	20.0	0.01	0.13±0.03	31.3±8.7	249.0±48.0	0.9±1.0	1.4±1.0*	7.2±8.0	11.1±8.0*
Lup IV	0	0	8.0	0.3	2.26±0.60	139.0±79.8	61.4±31.2	0.9±1.0*	1.4±1.0*	0.4±0.4*	0.6±0.4*
Lup IV	0	0	14.0	0.02	0.17±0.04	26.0±9.2	156.6±36.5	0.9±1.0*	1.4±1.0*	5.5±6.0*	8.4±6.0*
Lup IV	0	0	23.0	0.01	0.09±0.02	24.3±7.8	266.8±46.9	0.9±1.0*	1.4±1.0*	10.0±11.0*	15.3±11.0*
Oph	0	2	10.5	5.6	26.61±10.64	2323.2±1421.2	87.3±40.4	0.9±1.0*	2.8±1.5	0.03±0.04*	0.1±1.4
Oph	1	3	18.0	0.4	1.86±0.75	368.1±170.7	197.4±46.3	0.9±1.0	4.2±2.2	0.5±0.5	2.2±1.7
Oph	5	5	25.5	0.1	0.57±0.23	182.3±80.1	319.6±58.1	4.5±2.5	6.9±3.7	8.0±5.4	12.2±8.2
Oph	9	14	33.0	0.1	0.34±0.14	147.5±63.8	436.7±72.0	8.2±4.5	19.4±10.5	24.2±16.4	57.6±38.6
Oph	10	12	41.0	0.04	0.17±0.07	94.3±40.8	541.8±89.8	9.1±5.0	16.7±9.0	52.2±35.4	95.8±64.2
Per	3	0	6.5	2.7	52.28±20.91	3504.2±2158.9	67.0±31.4	2.7±1.5	1.4±1.0*	0.1±1.7	0.03±0.02*
Per	15	4	11.0	0.8	15.39±6.16	1880.9±910.5	122.2±33.3	13.6±7.5	5.6±3.0	0.9±3.9	0.4±2.0
Per	18	14	15.5	0.2	3.79±1.52	734.4±331.1	193.6±40.3	16.4±9.0	19.4±10.5	4.3±4.2	5.1±3.7
Per	28	11	20.0	0.1	1.49±0.60	388.8±170.4	260.3±46.7	25.5±13.9	15.3±8.2	17.0±11.6	10.2±6.9
Per	8	1	24.5	0.01	0.22±0.09	69.8±30.2	316.9±52.8	7.3±4.0	1.4±1.0	33.0±22.4	6.3±4.5
Per	0	0	30.0	0.001	0.02±0.01	7.2±3.2	403.0±81.0	0.9±1.0*	1.4±1.0*	50.9±56.0*	77.8±56.0*
Ser	2	1	10.2	0.6	13.34±1.03	1588.5±479.4	119.1±34.7	1.8±1.0	1.4±1.0	0.1±1.4	0.1±0.1
Ser	2	2	14.5	0.1	2.54±0.20	456.7±104.0	179.9±38.5	1.8±1.0	2.8±1.5	0.7±1.4	1.1±1.4
Ser	7	5	18.8	0.04	0.91±0.07	221.5±44.3	243.2±44.9	6.4±3.5	6.9±3.7	7.0±3.9	7.6±4.1
Ser	20	9	23.0	0.01	0.23±0.02	70.1±13.3	306.6±53.3	18.2±9.9	12.5±6.7	79.6±44.0	54.7±29.8
Aur	19	6	8.8	1.8	48.05±9.61	4293.9±1001.2	89.4±10.7	17.3±9.4	8.3±4.5	0.4±4.4	0.2±2.4
Aur	20	15	15.5	0.1	1.77±0.35	274.0±60.1	154.9±13.9	18.2±9.9	20.8±11.2	10.3±6.0	11.8±6.8
Aur	2	1	22.2	0.01	0.18±0.04	49.7±11.8	282.8±35.8	1.8±1.0	1.4±1.0	10.4±6.0	7.9±5.7
AurN	0	0	5.2	0.01	0.46±0.09	30.9±7.8	67.4±10.4	0.9±1.0*	1.4±1.0*	2.0±2.2*	3.0±2.2*
AurN	1	0	8.3	0.1	1.95±0.39	193.0±44.2	98.8±11.0	0.9±1.0	1.4±1.0*	0.5±0.5	0.7±0.5*
Cep	13	3	7.5	1.3	35.77±35.77	2327.7±597.5	331.9±52.1	11.8±7.5	4.2±3.0	0.3±0.2	0.1±0.1
Cep	13	3	13.0	0.1	2.21±2.21	282.6±63.3	507.2±51.3	11.8±7.0	4.2±3.0	5.4±3.3	1.9±1.4
Cha I	3	6	8.0	0.6	7.44±1.49	544.1±136.0	73.1±11.0	2.7±1.5	8.3±4.5	0.4±1.7	1.1±2.4
Cha I	7	5	14.0	0.1	1.75±0.35	256.0±57.5	146.6±15.0	6.4±3.5	6.9±3.7	3.6±2.6	4.0±2.3
Cha I	0	1	21.0	0.02	0.22±0.04	56.0±13.1	253.6±30.9	0.9±1.0*	1.4±1.0	4.1±4.5*	6.3±4.5
Cha III	1	0	5.0	2.2	26.85±5.37	1228.5±364.1	45.8±10.0	0.9±1.0	1.4±1.0*	0.03±0.04	0.05±0.04*
Cha III	0	0	8.0	0.1	1.14±0.23	97.5±23.0	85.2±10.6	0.9±1.0*	1.4±1.0*	0.8±0.9*	1.2±0.9*
CrA	2	1	9.3	0.5	2.45±0.94	162.8±68.1	66.5±11.0	1.8±1.0	1.4±1.0	0.7±1.4	0.6±0.4
CrA	1	2	16.7	0.09	0.47±0.18	87.2±34.7	183.5±18.2	0.9±1.0	2.8±1.5	1.9±2.1	5.8±3.9
CrA	4	0	24.0	0.02	0.10±0.04	29.1±11.6	289.8±28.4	3.6±2.0	1.4±1.0*	36.2±24.2	13.8±9.9*
IC5146E	0	0	4.7	0.2	50.60±8.52	2424.3±673.2	47.9±10.6	0.9±1.0*	1.4±1.0*	0.02±0.02*	0.03±0.02*
IC5146E	11	6	7.4	0.04	10.82±1.82	940.8±204.1	86.9±11.9	10.0±5.5	8.3±4.5	0.9±3.3	0.8±2.4
IC5146NW	7	0	5.5	0.3	73.75±12.42	3831.8±989.0	52.0±10.2	6.4±3.5	1.4±1.0*	0.1±2.6	0.02±0.01*
IC5146NW	8	3	9.0	0.05	13.83±2.33	1346.3±275.4	97.3±11.3	7.3±4.0	4.2±2.2	0.5±2.8	0.3±1.7
Lup V	0	0	4.5	1.3	9.08±2.42	514.5±166.2	56.7±10.3	0.9±1.0*	1.4±1.0*	0.1±0.1*	0.2±0.1*
Lup V	0	0	7.0	0.4	2.57±0.69	190.0±57.5	73.9±10.6	0.9±1.0*	1.4±1.0*	0.4±0.4*	0.5±0.4*
Lup VI	0	0	4.5	0.6	3.83±1.02	237.4±75.4	62.0±10.7	0.9±1.0*	1.4±1.0*	0.2±0.3*	0.4±0.3*
Lup VI	0	0	9.0	0.4	2.90±0.77	216.4±65.8	74.6±10.9	0.9±1.0*	1.4±1.0*	0.3±0.3*	0.5±0.3*
Mus	1	0	4.5	0.8	5.86±1.47	259.2±88.0	44.2±10.2	0.9±1.0	1.4±1.0*	0.2±0.2	0.2±0.2*
Mus	0	0	7.0	0.1	0.95±0.24	75.4±21.4	79.1±10.7	0.9±1.0*	1.4±1.0*	1.0±1.0*	1.5±1.0*
Sco	1	1	7.5	1.2	6.35±6.35	484.7±130.6	456.4±63.9	0.9±1.0	1.4±1.0	0.1±0.2	0.2±0.2
Sco	1	0	17.0	0.2	0.94±0.94	135.8±34.3	567.1±57.6	0.9±1.0	1.4±1.0*	1.0±1.1	1.5±1.1*
Ser-Aqu	0	0	7.0	3.0	61.01±4.69	5509.9±782.3	90.3±10.8	0.9±1.0*	1.4±1.0*	0.02±0.02*	0.02±0.02*
Ser-Aqu	9	4	12.0	4.6	95.23±7.33	12818.2±1540.2	134.6±12.4	8.2±4.5	5.6±3.0	0.1±3.0	0.1±2.0

TABLE 2—*Continued*

Cloud	$N_{\text{YSOs,I}}$	$N_{\text{YSOs,F}}$	Contour levels ¹ (mag)	Ω (deg ²)	A_{con} (pc ²)	M_{con} (M_{\odot})	$\Sigma_{\text{gas,con}}$ (M_{\odot} pc ⁻²)	SFR, I (M_{\odot} Myr ⁻¹)	SFR, F (M_{\odot} Myr ⁻¹)	$\Sigma_{\text{SFR,I}}$ (M_{\odot} yr ⁻¹ kpc ⁻²)	$\Sigma_{\text{SFR,F}}$ (M_{\odot} yr ⁻¹ kpc ⁻²)
(1)	(2)	(3)	(4)	(5)	(6)	(7)	(8)	(9)	(10)	(11)	(12)
Ser-Aqu	16	12	17.0	0.6	12.57±0.97	2658.5±298.5	211.4±17.3	14.5±8.0	16.7±9.0	1.2±4.0	1.3±3.5
Ser-Aqu	31	20	22.0	0.3	6.66±0.51	1929.6±219.8	289.6±24.3	28.2±15.4	27.8±15.0	4.2±5.6	4.2±4.5
Ser-Aqu	31	25	27.0	0.1	2.88±0.22	1036.8±125.3	359.6±33.5	28.2±15.4	34.7±18.7	9.8±5.6	12.0±6.6
Ser-Aqu	50	24	33.0	0.1	1.10±0.08	488.4±65.1	442.5±48.2	45.5±24.9	33.3±18.0	41.2±22.8	30.2±16.4
Contour Averages	6.6±1.2	4.1±0.7	-999.0±-999.0	0.6±0.1	10.6±2.5	972.1±248.0	188.1±17.7	6.0±1.1	5.7±1.0	7.7±2.0	8.6±2.3

Note. — Columns are : (1) Cloud name.; (2) Number of Class I YSOs in contour level.; (3) Number of Flat SED YSOs in contour level.; (4) A_V contour level in mag at which mass measurement was made. The contour levels start at $A_V=2$ or the cloud completeness limit and increase in even intervals to the listed contour level.; (5) Solid angle.; (6) Area in contour level (pc⁻²).; (7) Mass in contour level (M_{\odot}).; (8) Surface gas density in contour level (M_{\odot} pc⁻²).; (9) Star formation rate in contour level (M_{\odot} Myr⁻¹) for Class I YSOs. Asterisks denote that measurement is an upper limit.; (10) Star formation rate in contour level (M_{\odot} Myr⁻¹) for Flat SED YSOs. Asterisks denote that measurement is an upper limit.; (11) Star formation rate density in contour level (M_{\odot} yr⁻¹ kpc⁻²) for Class I YSOs. Asterisks denote that measurement is an upper limit.; (12) Star formation rate density in contour level (M_{\odot} (yr⁻¹ kpc⁻²) for Flat SED YSOs. Asterisks denote that measurement is an upper limit.; (I) Contour levels start at $A_V = 2$ for all clouds except for Serpens and Ophiuchus which are covered by the c2d survey completely down to $A_V = 6$ and 3 as discussed in Section 2.1.

TABLE 3
PROPERTIES OF SUSPICIOUS YSOs AND MISFITS

Cloud	RA	DEC	Classification	α	$\int T_{\text{MB}} dV$	T_{MB}	SED	A_V	comments
(1)	J2000	J2000	(4)	(5)	(K km s ⁻¹)	(K)	class	(mag)	(10)
Aur	04:18:21.27	+38:01:35.88	YSOc	-0.09		<0.23	Flat	4	
Aur	04:19:44.67	+38:11:21.98	YSOc_star+dust(IR1)	-0.07		<0.23	Flat	7	
Aur	04:29:40.02	+35:21:08.95	YSOc_star+dust(IR1)	0.51		<0.31	I	8	
Aur	04:30:14.96	+36:00:08.53	YSOc_red	1.77	0.42±0.09	0.69±0.15	I	8	
Aur	04:30:23.83	+35:21:12.35	YSOc_red	0.61		<0.30	I	8	
Aur	04:30:41.17	+35:29:41.08	YSOc_red	1.49	0.76±0.07	1.49±0.14	I	7	self-reversed
Aur	04:30:44.23	+35:59:51.16	YSOc	1.08	0.76±0.15	0.78±0.15	I	8	
Aur	04:30:48.52	+35:37:53.76	YSOc_red	1.46	1.01±0.13	1.15±0.15	I	7	self-reversed
Aur	04:30:56.62	+35:30:04.55	YSOc_red	2.35	0.49±0.07	1.00±0.15	I	7	
Cep	22:29:33.35	+75:13:16.01	YSOc_red	0.20		<0.42	Flat	6	
Cep	22:35:00.82	+75:15:36.42	YSOc_star+dust(IR2)	-0.29		<0.46	Flat	6	
Cep	22:35:14.09	+75:15:02.61	YSOc_red	0.36		<0.42	I	6	
Cep	21:01:36.07	+68:08:22.54	YSOc	-0.21		<0.42	I	5	
Cep	21:01:43.89	+68:14:03.31	YSOc_red	0.14		<0.40	I	6	
Cep	21:02:14.06	+68:07:30.80	YSOc_red	0.49		<0.40	I	6	
Cep	21:02:21.22	+67:54:20.28	YSOc_red	0.68	0.89± 0.18	1.74± 0.34	I	9	double peak
Cep	21:02:21.22	+67:54:20.28	YSOc_red	0.68	0.72± 0.11	2.33± 0.34	I	9	double peak
Cep	21:02:21.36	+68:04:36.11	YSOc_PAH-em	0.52		<0.42	I	5	
Cep	21:02:59.46	+68:06:32.24	YSOc_red	0.65		<0.42	I	5	
IC5146E	21:52:46.58	+47:12:49.32	YSOc_star+dust(IR2)	-0.19		<0.34	Flat	5	
IC5146E	21:53:36.24	+47:10:27.84	YSOc_star+dust(IR1)	-0.12		<0.30	Flat	6	
IC5146E	21:54:18.76	+47:12:09.73	YSOc_star+dust(IR2)	-0.23		<0.26	Flat	4	
IC5146E	21:52:14.36	+47:14:54.60	YSOc_star+dust(IR2)	0.67		<0.28	I	4	
IC5146E	21:52:37.78	+47:14:38.40	YSOc_star+dust(IR1)	0.64	1.59± 0.25	1.80± 0.28	I	5	
IC5146E	21:53:06.94	+47:14:34.80	YSOc	0.34	0.71± 0.27	0.66± 0.25	I	5	
IC5146E	21:53:55.70	+47:20:30.13	YSOc_PAH-em	1.59		<0.34	I	4	
IC5146NW	21:45:31.22	+47:36:21.24	YSOc	0.13	0.44± 0.19	0.61± 0.26	Flat	5	
IC5146NW	21:44:43.08	+47:46:43.68	YSOc_red	0.63	1.92± 0.11	4.18± 0.23	I	4	
IC5146NW	21:44:48.31	+47:44:59.64	YSOc_red	1.83	0.65± 0.05	3.11± 0.23	I	5	
IC5146NW	21:44:53.98	+47:45:43.56	YSOc_star+dust(IR1)	0.76	0.70± 0.11	1.75± 0.28	I	4	
IC5146NW	21:45:02.64	+47:33:07.56	YSOc_red	1.18	0.77± 0.22	1.03± 0.30	I	4	
IC5146NW	21:45:08.31	+47:33:05.77	YSOc_red	0.74	3.72± 0.53	2.07± 0.30	I	4	
IC5146NW	21:45:27.86	+47:45:50.40	YSOc_star+dust(IR4)	0.42		<0.36	I	3	
IC5146NW	21:47:06.02	+47:39:39.24	YSOc_red	0.43	0.40± 0.14	0.70± 0.25	I	5	
Lup I	15:38:48.35	-34:40:38.24	YSOc_PAH-em	0.31		<0.42	I	3	
Lup I	15:43:02.29	-34:44:06.22	YSOc_star+dust(IR1)	0.14		<0.38	Flat	<2	
Lup III	16:07:03.85	-39:11:11.59	YSOc_star+dust(IR1)	-0.14		<0.30	Flat	<2	
Lup III	16:07:08.57	-39:14:07.75	YSOc	-0.01		<0.32	Flat	<2	
Lup III	16:07:54.73	-39:15:44.49	YSOc_red	-0.15		<0.28	Flat	2	
Lup IV	16:02:21.61	-41:40:53.70	YSOc_PAH-em	0.56		<0.36	I	4	
Lup VI	16:24:51.78	-39:56:32.66	YSOc	0.22		<0.48	Flat	8	
Oph	16:21:38.72	-22:53:28.26	YSOc_star+dust(IR1)	0.99		<0.35	I	<3	
Oph	16:23:40.00	-23:33:37.36	YSOc	0.01		<0.37	Flat	3	
Oph	16:44:24.27	-24:01:24.56	YSOc_PAH-em	0.27		<0.35	Flat	<3	
Oph	16:45:26.65	-24:03:05.41	YSOc_red	0.37		<0.36	I	<3	
Oph	16:21:45.13	-23:42:31.63	YSOc_star+dust(IR1)	0.30		<0.36	I	9	
Oph	16:31:31.24	-24:26:27.87	YSOc_star+dust(IR4)	-0.24		<0.38	Flat	<3	
Oph	16:25:27.56	-24:36:47.55	YSOc_star+dust(IR1)	0.06		<0.42	Flat	7	
Oph	16:23:32.22	-24:25:53.82	YSOc_star+dust(IR2)	-0.04	0.36± 0.17	0.66± 0.31	Flat	4	
Oph	16:22:20.99	-23:04:02.35	YSOc_PAH-em	0.17		<0.44	Flat	4	
Oph	16:23:05.43	-23:02:56.73	YSOc_star+dust(IR2)	-0.27		<0.46	Flat	4	
Oph	16:23:06.86	-22:57:36.61	YSOc	-0.19		<0.44	Flat	5	
Oph	16:23:40.00	-23:33:37.36	YSOc	0.01		<0.46	Flat	4	
Per	03:25:19.52	+30:34:24.16	YSOc	-0.11		<0.27	Flat	2	
Per	03:26:37.47	+30:15:28.08	YSOc_red	0.99	0.20±0.04	0.77±0.14	I	2	double peak
Per	03:26:37.47	+30:15:28.08	YSOc_red	0.99	0.11±0.03	0.49±0.14	I	2	double peak
Per	03:28:34.49	+31:00:51.10	YSOc_star+dust(IR1)	0.89	0.31±0.05	0.95±0.15	I	6	
Per	03:28:34.94	+30:54:54.55	YSOc	0.01		<0.32	Flat	3	
Per	03:29:06.05	+30:30:39.19	YSOc_red	0.72		<0.30	I	2	
Per	03:29:51.82	+31:39:06.03	red	3.34	3.22±0.20	2.41±0.15	I	6	
Per	03:30:22.45	+31:32:40.53	YSOc_star+dust(IR2)	0.35		<0.34	I	3	
Per	03:30:38.21	+30:32:11.93	YSOc_star+dust(IR2)	-0.10		<0.29	Flat	4	
Per	03:31:14.70	+30:49:55.40	YSOc_star+dust(IR1)	-0.09		<0.30	Flat	2	
Per	03:31:20.98	+30:45:30.06	YSOc_red	1.10	2.70±0.17	2.68±0.17	I	5	
Per	03:44:24.84	+32:13:48.36	YSOc_red	1.69		<0.31	I	6	
Per	03:44:35.34	+32:28:37.18	YSOc_red	-0.09		<0.32	Flat	3	
Per	03:45:13.82	+32:12:10.00	YSOc_red	0.43		<0.28	I	3	
Per	03:47:05.43	+32:43:08.53	YSOc_red	0.48	0.93±0.09	1.48±0.14	I	5	
Sco	16:46:58.27	-09:35:19.76	YSOc_red	0.66		<0.44	I	12	
Sco	16:48:28.85	-14:14:36.45	YSOc_PAH-em	0.48		<0.48	I	5	
Sco	16:22:04.35	-19:43:26.76	YSOc	0.02		<0.66	Flat	6	
Ser	18:28:41.87	-00:03:21.34	YSOc_star+dust(IR1)	0.14		<0.47	Flat	8	
Ser	18:28:44.78	+00:51:25.79	YSOc_red	1.05	0.86±0.23	0.83±0.22	I	8	
Ser	18:28:44.96	+00:52:03.54	YSOc_red	1.27	1.61±0.34	1.36±0.28	I	8	
Ser	18:29:16.18	+00:18:22.71	YSOc	-0.13	1.28±0.29	0.98±0.22	Flat	7	
Ser	18:29:40.20	+00:15:13.11	YSOc_star+dust(IR1)	0.68		<0.50	I	<6	
Ser	18:30:05.26	+00:41:04.58	red	1.24		<0.44	I	<6	
Ser	18:28:44.01	+00:53:37.93	YSOc_red	0.29		<0.42	Flat	7	

TABLE 3—*Continued*

Cloud	RA	DEC	Classification	α	$\int T_{\text{MB}} dV$	T_{MB}	SED	A_V	comments
(1)	J2000 (2)	J2000 (3)	(4)	(5)	(K km s ⁻¹) (6)	(K) (7)	class (8)	(mag) (9)	(10)
Ser	18:29:27.35	+00:38:49.75	YSOc	0.24		<0.38	Flat	13	
Ser	18:29:31.96	+01:18:42.91	YSOc_star+dust(IR1)	0.32	0.63± 0.27	0.69± 0.30	I	11	
Ser-Aqu	18:13:45.05	-03:26:02.67	YSOc_star+dust(IR1)	0.39		<0.58	I	6	
Ser-Aqu	18:27:03.33	-02:45:33.42	YSOc_red	0.44		<0.54	I	5	
Ser-Aqu	18:29:16.80	-01:17:30.68	YSOc	0.78		<0.54	I	10	
Ser-Aqu	18:30:32.48	-03:50:01.21	YSOc_star+dust(MP1)	0.37		<0.54	I	9	
Ser-Aqu	18:33:03.49	-02:08:42.53	YSOc_PAH-em	1.25		<0.56	I	8	
Ser-Aqu	18:37:39.24	-00:25:35.18	YSOc_star+dust(IR1)	0.72		<0.56	I	7	
Ser-Aqu	18:37:46.90	-00:01:55.83	YSOc_PAH-em	1.19		<0.52	I	8	
Ser-Aqu	18:37:52.77	-00:23:03.10	YSOc_star+dust(MP1)	0.59		<0.50	I	7	
Ser-Aqu	18:37:55.79	-00:23:31.59	YSOc	1.14		<0.58	I	8	
Ser-Aqu	18:05:31.11	-04:38:09.63	YSOc	0.23		<0.60	Flat	9	
Ser-Aqu	18:10:28.90	-02:37:42.79	YSOc	-0.18		<0.62	Flat	6	
Ser-Aqu	18:26:32.81	-03:46:27.26	YSOc_red	0.08		<0.60	Flat	10	
Ser-Aqu	18:27:24.87	-03:58:21.15	YSOc	-0.22		<0.60	Flat	10	
Ser-Aqu	18:28:09.49	-02:26:31.95	YSOc_star+dust(IR2)	-0.11		<0.58	Flat	5	
Ser-Aqu	18:29:16.72	-01:17:36.92	YSOc_star+dust(MP1)	-0.08		<0.62	Flat	10	
Ser-Aqu	18:30:06.06	-01:10:19.33	YSOc	-0.15		<0.56	Flat	6	
Ser-Aqu	18:30:13.01	-01:25:36.64	YSOc_star+dust(IR2)	-0.23		<0.60	Flat	8	
Ser-Aqu	18:36:02.64	-00:02:20.70	YSOc_star+dust(MP1)	-0.28		<0.58	Flat	8	
Ser-Aqu	18:38:55.77	-00:23:40.81	YSOc	-0.05		<0.64	Flat	7	
Ser-Aqu	18:40:12.06	+00:29:27.74	YSOc_red	-0.07		<0.50	Flat	8	

Note. — Columns are : (1) Cloud (2) Source Right Ascension in J2000 coordinates; (3) Source Declination in J2000 coordinates; (4) Source classification (see Evans et al. (2009)); (5) Spectral Index, extinction corrected values for c2d clouds only; (6) Integrated main beam HCO⁺line intensity; (7) Main beam HCO⁺line temperature, upper limits are computed as $2\sigma_{\text{rms}}$; (8) SED class based on Greene et al. (1994); (9) A_V in source position. Values that are found outside the A_V map completeness limit are given as < limit; (10) Line profile comments.

TABLE 4
 A_V , ^{12}CO , AND ^{13}CO MASSES AND Σ_{gas} FOR PER AND OPH CLOUDS

Cloud	$M_{\text{cloud,gas}}$ (M_{\odot})	$M_{\text{cloud},^{12}\text{CO}}$ (M_{\odot})	$M_{\text{cloud},^{13}\text{CO}}$ (M_{\odot})	$\Sigma_{\text{cloud,gas}}$ (M_{\odot} pc ⁻²)	$\Sigma_{\text{cloud},^{12}\text{CO}}$ (M_{\odot} pc ⁻²)	$\Sigma_{\text{cloud},^{13}\text{CO}}$ (M_{\odot} pc ⁻²)
(1)	(2)	(3)	(4)	(5)	(6)	(7)
Per	5997±3387	9657±2416	1073±110	82±33	132±33	15±2
Oph	2270±1533	2596±659	348±39	77±42	88±22	12±1
Data from Literature:						
Taurus ^I	27207	16052		108	64	

Note. — (1) Cloud name.; (2) Mass from A_V map (M_{\odot}) where there is positive ^{12}CO and ^{13}CO emission.; (3) ^{12}CO Mass (M_{\odot}); (4) ^{13}CO Mass (M_{\odot}); (5) Surface gas density from A_V map (M_{\odot} pc⁻²); (6) ^{12}CO Surface gas density (M_{\odot} pc⁻²); (7) ^{13}CO Surface gas density (M_{\odot} pc⁻²); (I) Combined ^{12}CO and ^{13}CO mass from Goldsmith et al. (2008) and A_V mass from (Pineda et al. 2010).

TABLE 5
 A_V , ^{12}CO , AND ^{13}CO MASSES AND Σ_{gas} FOR PER AND OPH CLOUDS IN A_V CONTOURS

Cloud	Contour levels (mag)	$M_{\text{con,gas}}$ (M_{\odot})	$M_{\text{con},^{12}\text{CO}}$ (M_{\odot})	$M_{\text{con},^{13}\text{CO}}$ (M_{\odot})	$\Sigma_{\text{con,gas}}$ ($M_{\odot} \text{ pc}^{-2}$)	$\Sigma_{\text{con},^{12}\text{CO}}$ ($M_{\odot} \text{ pc}^{-2}$)	$\Sigma_{\text{con},^{13}\text{CO}}$ ($M_{\odot} \text{ pc}^{-2}$)
(1)	(2)	(3)	(4)	(5)	(6)	(7)	(8)
Per	6.5	3144.7±2068.5	6050.8±1514.5	518.0±54.0	60.2±31	115.7±28	9.9±1
	11.0	1774.0±875.5	2555.9±639.3	349.1±35.3	115.3±33	166.1±41	22.7±2
	15.5	652.9±302.6	654.0±163.6	120.3±12.1	172.1±40	172.4±43	31.7±3
	20.0	369.7±163.5	343.7±86.0	76.2±7.6	247.6±46	230.2±57	51.0±5
	24.5	49.5±23.0	49.4±12.4	8.9±0.9	224.9±52	224.5±56	40.5±4
Oph	30.0	6.1±2.8	3.3±0.8	0.7±0.1	339.3±80	187.7±46	37.6±3
	10.5	1577.2±1246.7	1982.0±505	183.3±23	76.8±40	74.5±19	6.9±0
	18.0	349.4±164.3	328.4±82	71.1±7	187.4±46	176.1±44	38.1±3
	25.5	161.3±72.5	135.9±34	42.6±4	282.8±58	238.3±59	74.7±7
	33.0	111.5±50.8	97.1±24	32.2±3	330.3±72	287.5±71	95.3±9
	41.0	70.6±32.3	52.9±13	18.6±1	405.9±89	304.0±76	106.6±10

Note. — (1) Cloud name.; (2) A_V contour level in mag at which mass measurement was made. The contour levels start at $A_V=2$ or the cloud completeness limit and increase in even intervals to the listed contour level.; (3) A_V Mass (M_{\odot}) where there is positive ^{12}CO and ^{13}CO emission.; (4) ^{12}CO Mass (M_{\odot}).; (5) ^{13}CO Mass (M_{\odot}).; (6) A_V Surface gas density ($M_{\odot} \text{ pc}^{-2}$).; (7) ^{12}CO Surface gas density ($M_{\odot} \text{ pc}^{-2}$).; (8) ^{13}CO Surface gas density ($M_{\odot} \text{ pc}^{-2}$).

TABLE 6
 MASSIVE CLUMPS $\text{HCN}J=(1-0)$

Source	$\log \Sigma_{\text{HCN}}$ ($M_{\odot} \text{ pc}^{-2}$)	$\log \Sigma_{\text{SFR,IR}}$ ($M_{\odot} \text{ yr}^{-1} \text{ kpc}^{-2}$)
(1)	(2)	(3)
W3(OH)	3.39±0.13	1.35±0.12
RCW142	3.40±0.14	1.08±0.13
W28A2(1)	3.66±0.14	2.12±0.13
G9.62+0.10	3.28±0.13	1.45±0.14
G10.60-0.40	3.32±0.12	1.83±0.12
G12.21-0.10	2.63±0.24	0.28±0.23
G13.87+0.28	2.28±0.15	0.61±0.13
G23.95+0.16	2.28±0.25	0.79±0.21
W43S	2.63±0.14	1.51±0.14
W44	2.79±0.18	1.00±0.16
G35.58-0.03	3.41±0.24	0.89±0.22
G48.61+0.02	1.98±0.14	0.75±0.13
W51M	3.14±0.17	1.53±0.17
S87	2.76±0.16	0.97±0.12
S88B	2.68±0.19	1.31±0.15
K3-50	3.26±0.12	1.75±0.13
ON1	2.83±0.14	0.73±0.13
ON2S	2.76±0.16	1.44±0.14
W75N	3.13±0.13	1.50±0.12
DR21S	3.20±0.13	1.75±0.12
W75(OH)	3.21±0.13	0.62±0.13
CEPA	3.44±0.17	2.00±0.13
IRAS20126	2.98±0.18	1.22±0.13
IRAS20220	2.63±0.21	0.29±0.18
IRAS23385	2.79±0.19	0.43±0.15
Clump Average	3.12±0.16	1.44±0.15

Note. — Columns are : (1) Source name (2) Surface gas density; (3) SFR surface gas density.

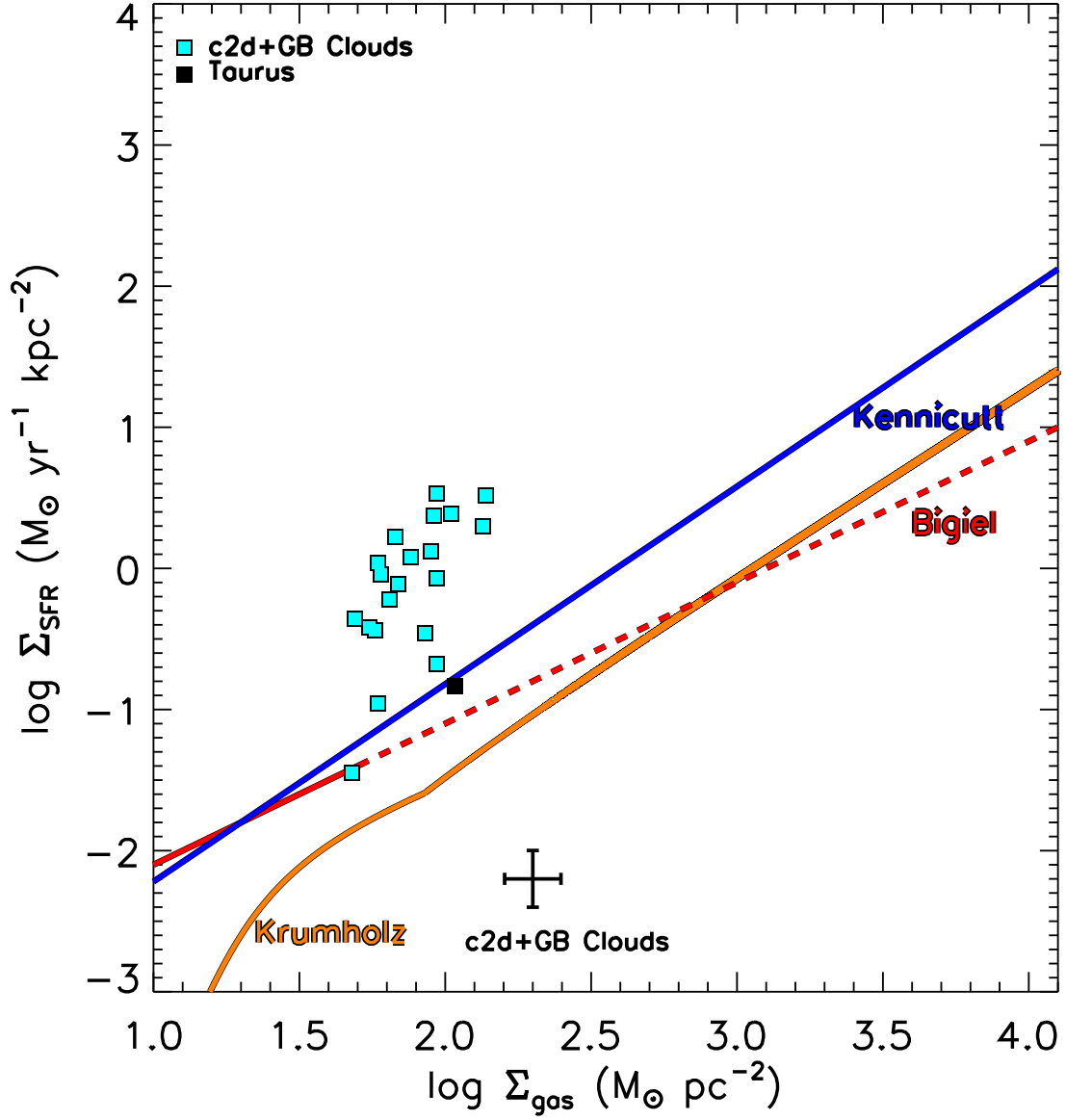


FIG. 1.— Σ_{SFR} is shown versus the Σ_{gas} for c2d and GB clouds (cyan squares). All cloud Σ_{gas} are measured above $A_V > 2$ (or the cloud completeness limit, see Section 2.1). We also include an estimate for the Taurus molecular cloud (black square) which includes YSO counts from Rebull et al. (2010) and an $A_V > 2$ gas mass from Pineda et al. (2010). Extragalactic observed relations are shown for the sample of Kennicutt (1998b) and Bigiel et al. (2008) (blue solid and red lines, respectively). The Krumholz et al. (2009) prediction for the total (H I+CO) gas star formation law for the galactic metallicity and a clumping factor of 1 corresponding to ~ 100 pc scales is also shown (orange line).

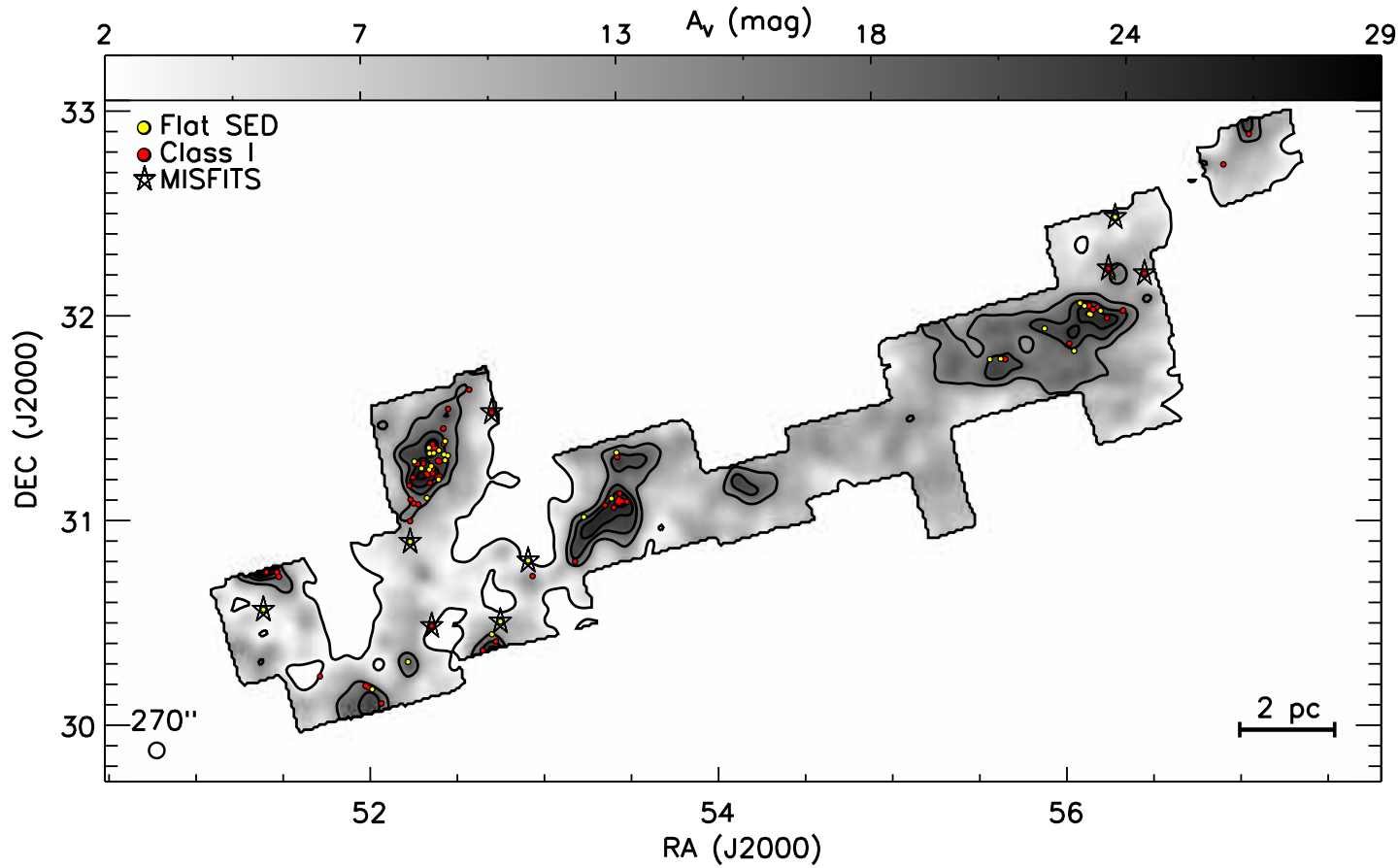


FIG. 2.— An example of the Σ_{gas} measurement method in the Perseus molecular cloud from the c2d survey. The grayscale image is the extinction map with black contours ranging from 2–29 in intervals of 4.5 mag. The yellow filled circles are Flat SED sources and the red filled circles are Class I sources. Sources that have an open star correspond to suspicious YSOs (MISFITS) that were observed in $\text{HCO}^+ J=3-2$ at the CSO and were not detected. We measure the Σ_{gas} from each map in each contour of extinction. Contours are spaced in intervals wider than the extinction map beam size of $270''$. To estimate SFR, we count the YSOs in corresponding contour levels (Section 2.2).

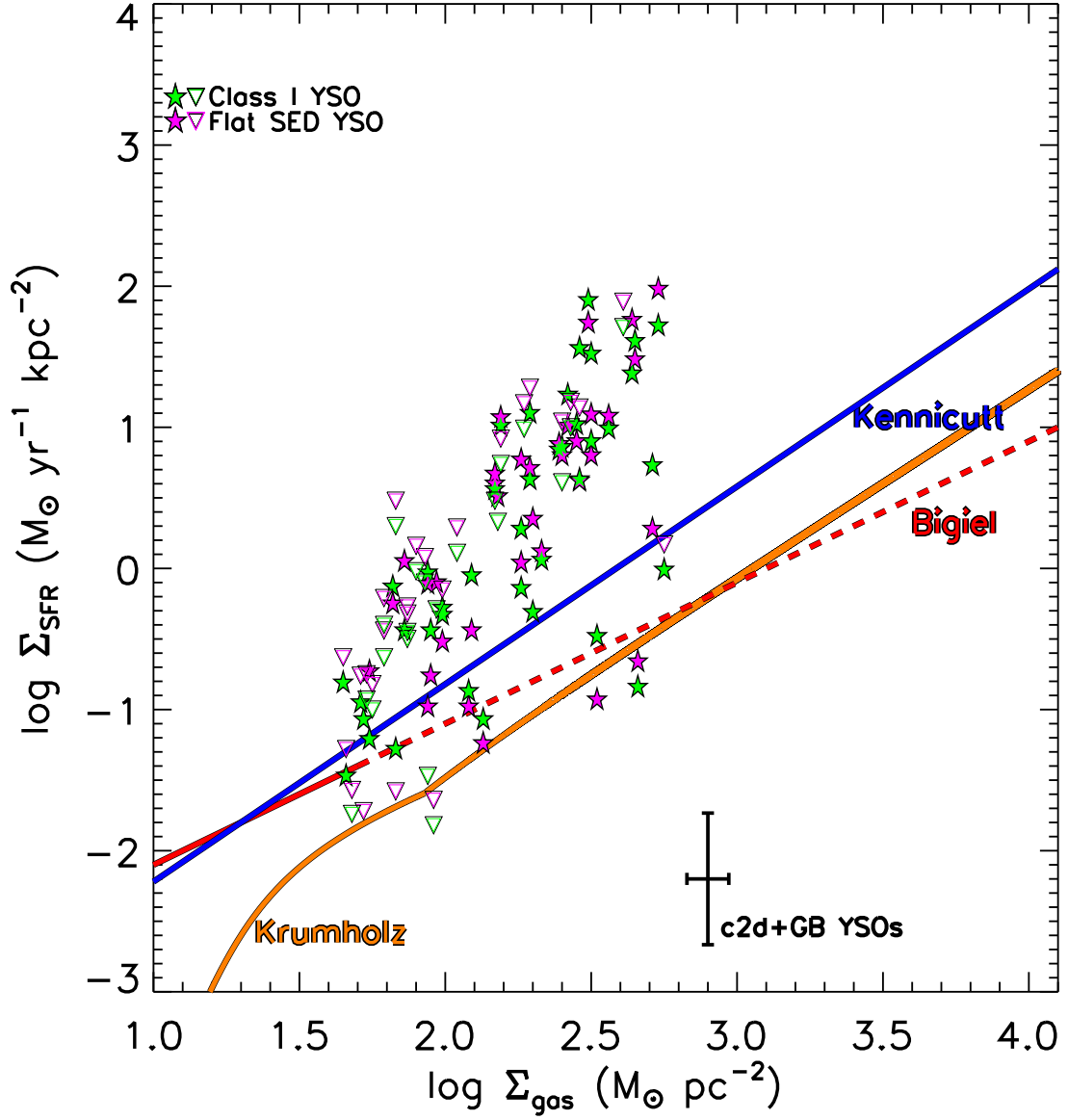


FIG. 3.— Gas surface densities measured from extinction maps and SFRs estimated from Class I (green stars) and Flat SED (magenta stars) YSO number counts in c2d and Gould’s belt clouds are shown. For contour levels that do not contain any YSOs, we calculate an upper limit for that region using one YSO (open inverted triangles). Extragalactic observed relations are shown for the sample of Kennicutt (1998b) and Bigiel et al. (2008) (blue solid and red lines, respectively).

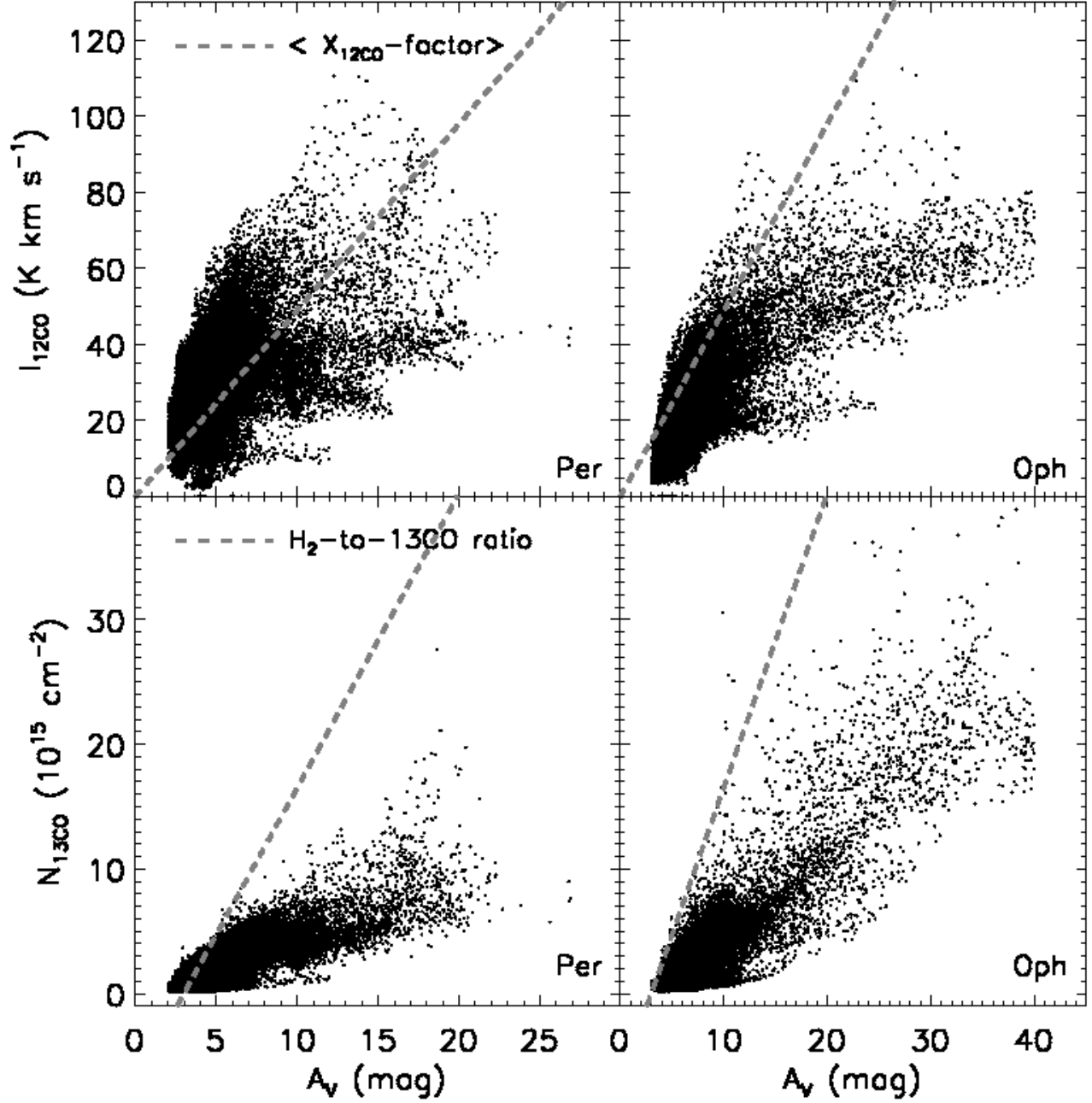


FIG. 4.— **top panels:** ^{12}CO integrated intensity versus visual extinction (A_V) for Per (left) and Oph (right). The standard X_{CO} -factor fit from Bloemen et al. (1986) is shown by the dashed grey lines (Section 3.1). **bottom panels:** ^{13}CO column densities versus visual extinction (A_V) for Per (left) and Oph (right). The average $\text{H}_2\text{-to-}^{13}\text{CO}$ abundance ratio from the literature is shown by the grey dashed lines (Section 3.1).

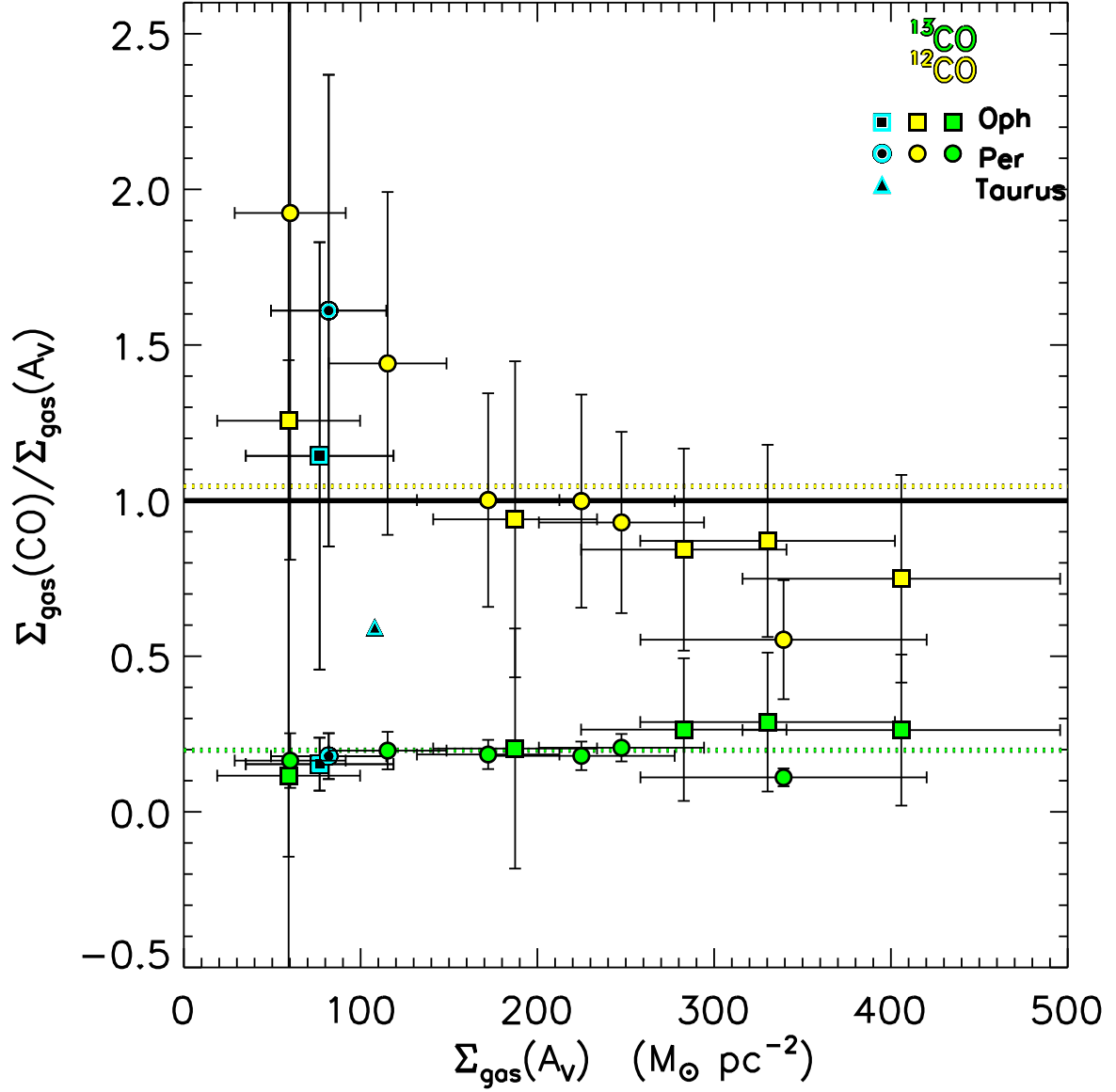


FIG. 5.— The ratio of H₂ gas surface densities from CO compare to that estimated from A_V maps (Σ_{gas}). The cyan squares and circles are points for the Oph and Per clouds, respectively. The filled green (^{13}CO) and yellow (^{12}CO) squares (Oph) and circles (Per) are measurements in evenly spaced contour intervals of A_V . The dashed horizontal green and yellow lines are the average of ^{13}CO and ^{12}CO contour points. If CO traces the mass we find using extinction maps, we would expect the ratio of CO/ A_V to be of order unity as shown by the solid black line.

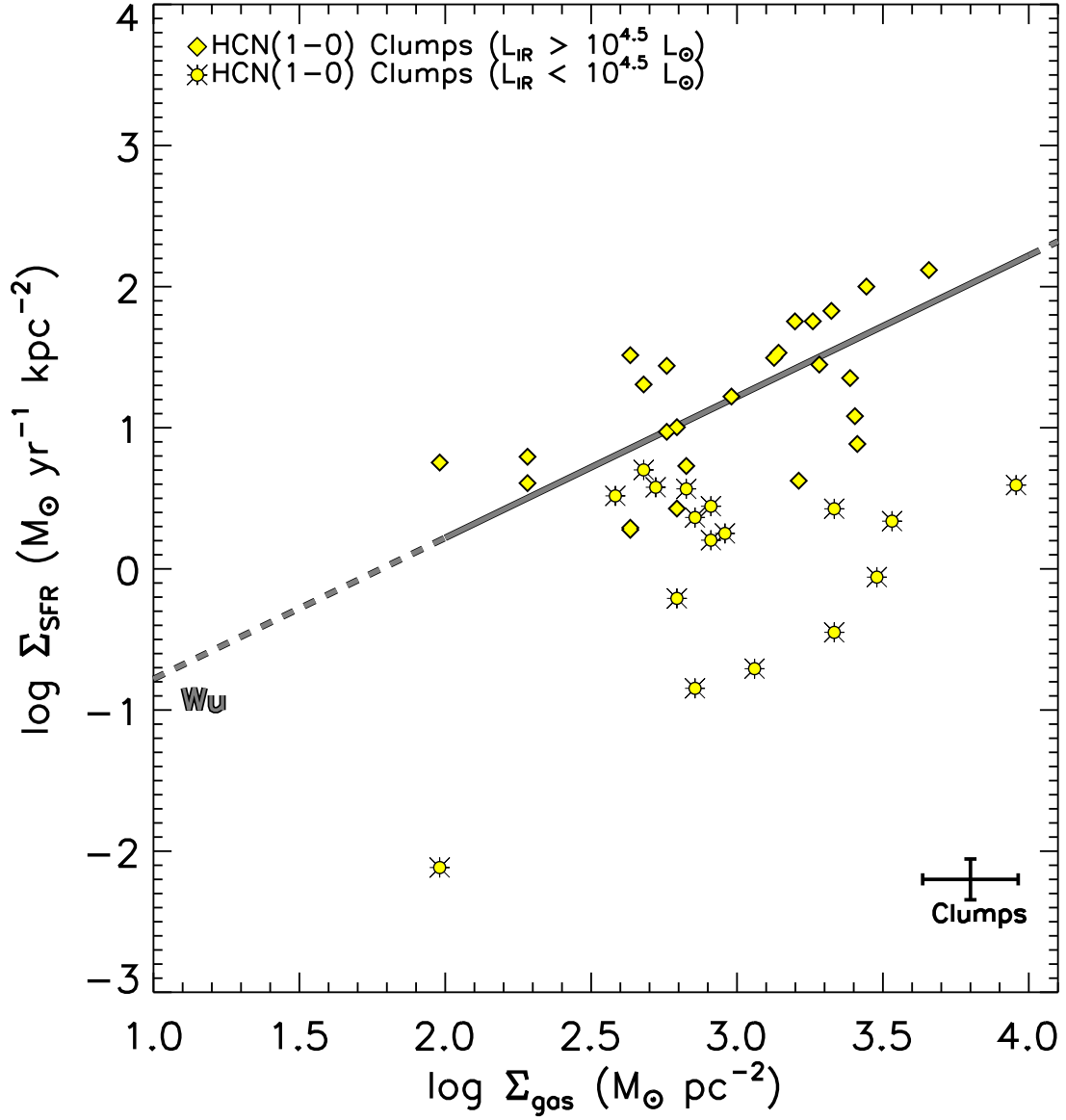


FIG. 6.— Σ_{gas} and Σ_{SFR} are shown for the sample of massive dense clumps from the survey of Wu et al. (2010). Gas surface densities are measured from the HCN $J=1-0$ maps and SFRs are estimated from the total IR luminosity, using the extragalactic prescription from Kennicutt (1998b). The relation between SFR and dense gas from Wu et al. (2005) is shown (grey solid line) and is extrapolated to lower Σ_{gas} . We make a cut at $L_{\text{IR}} > 10^{4.5} L_{\odot}$, below which the clumps are not massive enough to sample the IMF and lie off the linear relation (Section 3.2).

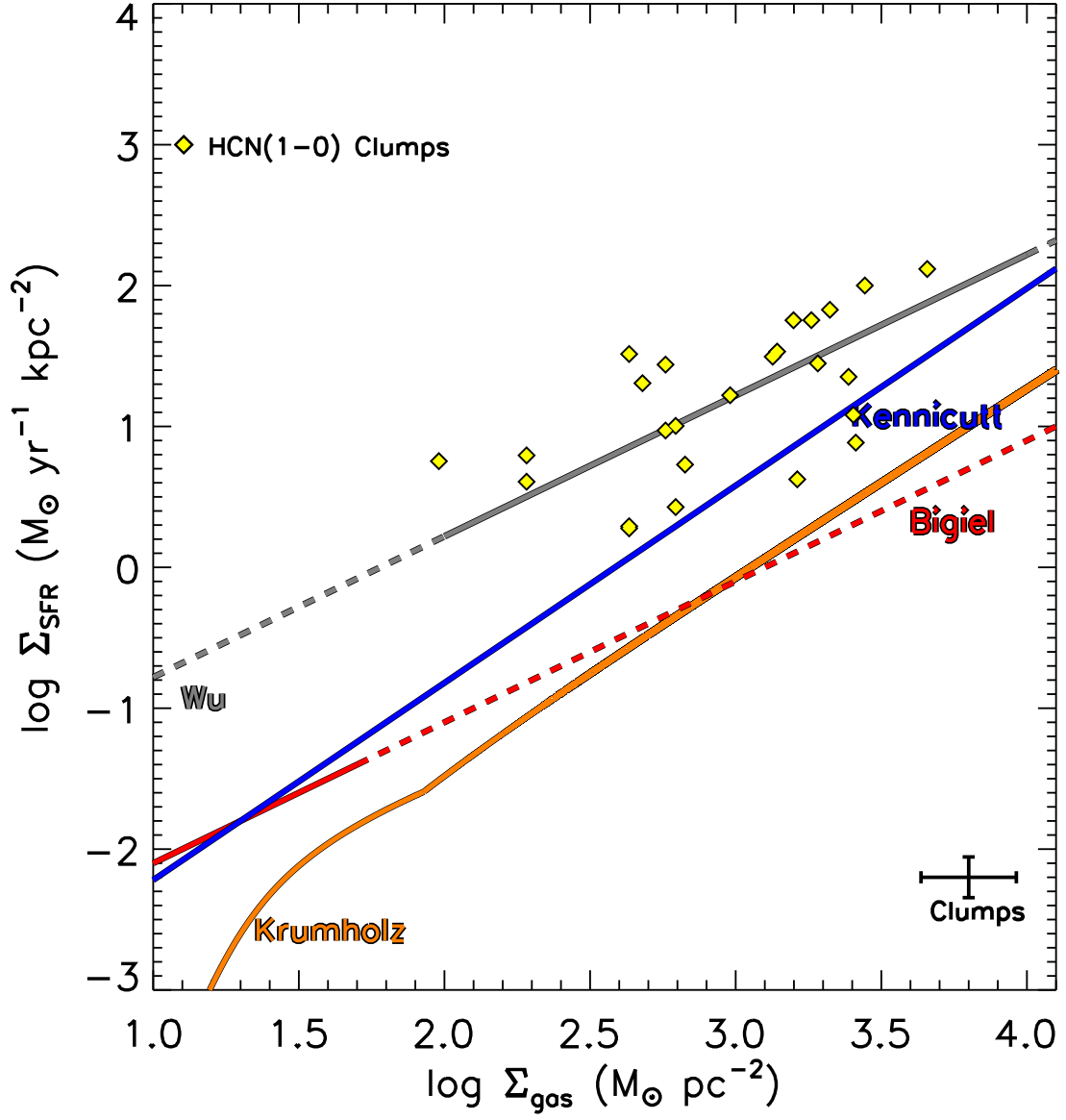


FIG. 7.— Comparison of massive, dense clumps with $L_{\text{IR}} > 10^{4.5} L_{\odot}$ to extragalactic relations (Kennicutt (1998b), Bigiel et al. (2008), and Krumholz et al. (2009), blue, red, and orange lines, respectively). The relation between SFR and dense gas from Wu et al. (2005) is also shown (grey solid line).

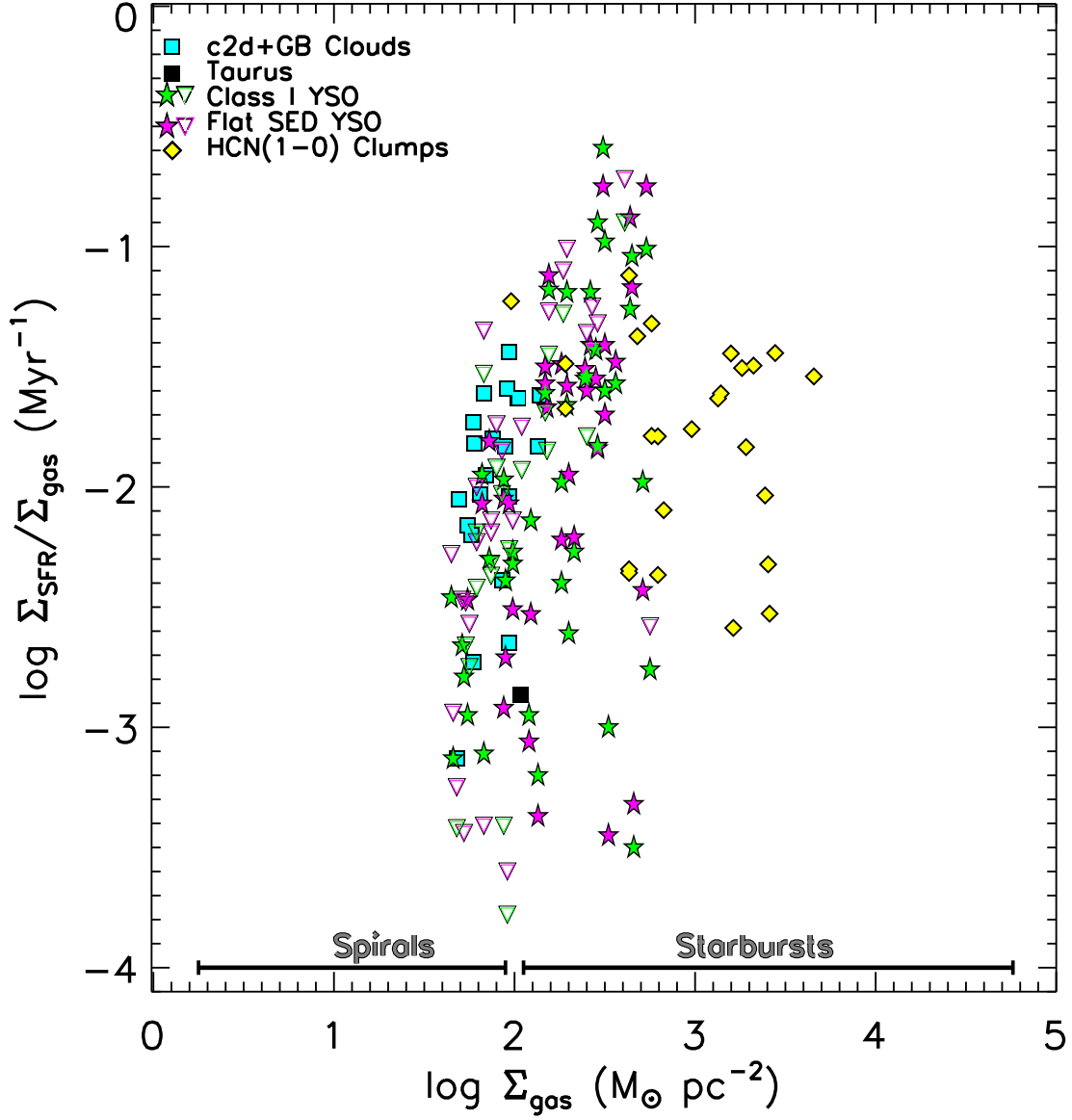


FIG. 8.— The ratio of Σ_{SFR} and Σ_{gas} compared to Σ_{gas} for low and high-mass star forming regions. We find a steep fall off in $\Sigma_{\text{SFR}}/\Sigma_{\text{gas}}$ in the range of $\Sigma_{\text{gas}} \sim 100\text{--}200 M_{\odot} \text{pc}^{-2}$. We denote this steep fall off as a star forming threshold, Σ_{th} , between active star forming regions and inactive regions.

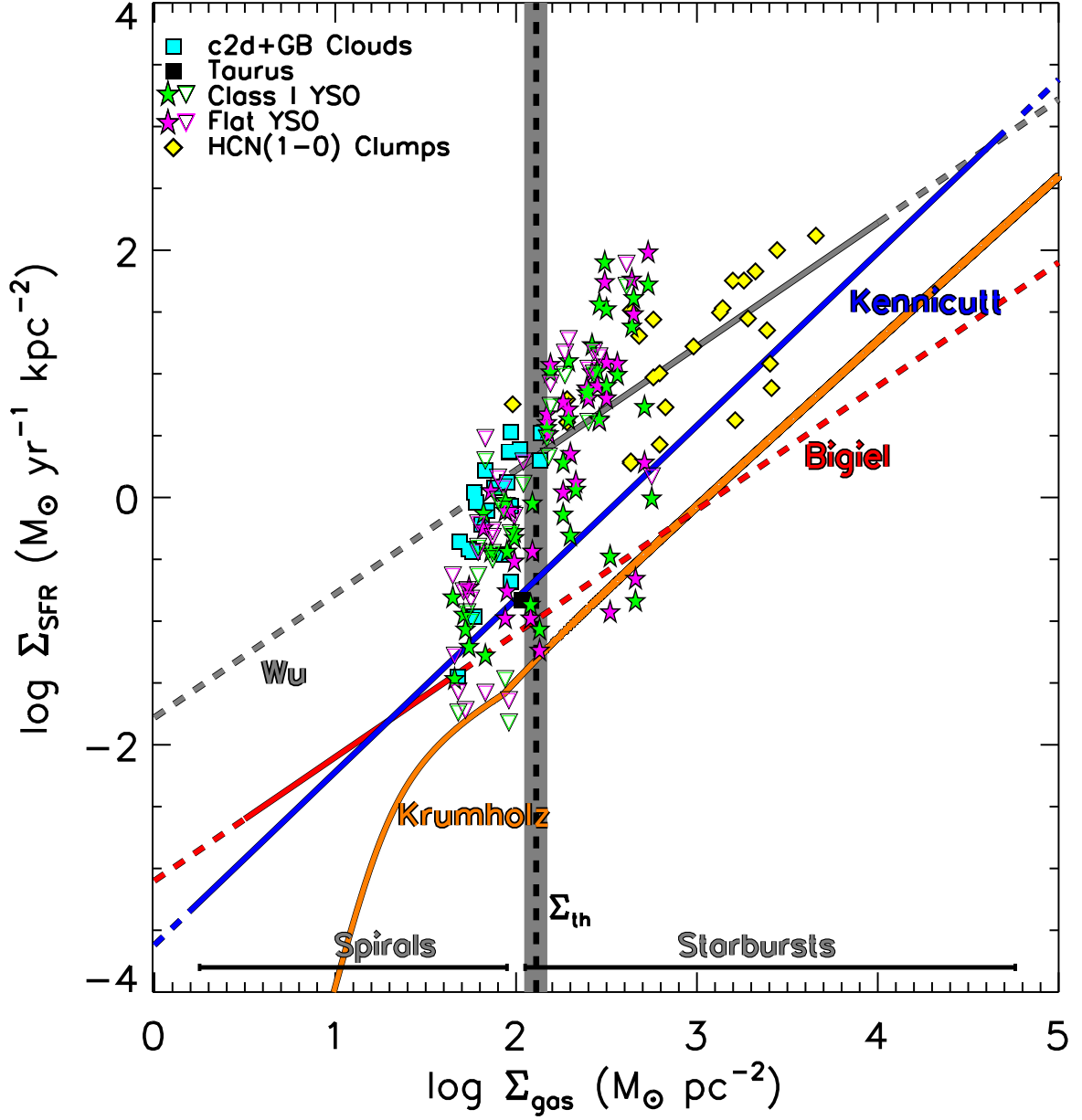


FIG. 9.— Comparison of Galactic total c2d and GB clouds, YSOs, and massive clumps to extragalactic relations. SFR and gas surface densities for the total c2d and GB clouds (cyan squares), c2d Class I and Flat SED YSOs (green and magenta stars), and $L_{\text{IR}} > 10^{4.5} L_{\odot}$ massive clumps (yellow diamonds) are shown. The range of gas surface densities for the spirals and circumnuclear starburst galaxies in the Kennicutt (1998b) sample are denoted by the grey horizontal lines. The grey shaded region denotes the range for Σ_{th} of $129 \pm 14 \text{ M}_{\odot} \text{ pc}^{-2}$.

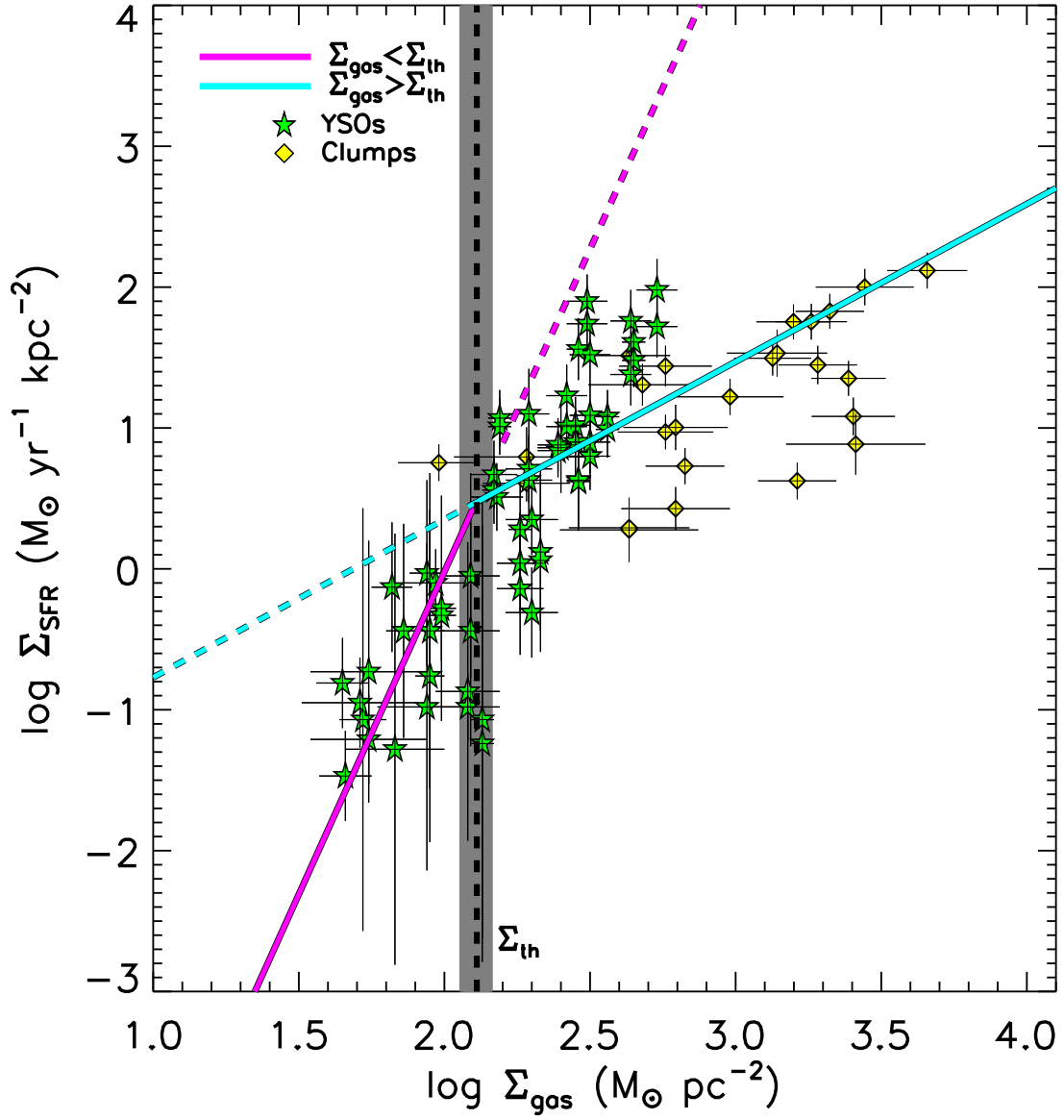


FIG. 10.— We fit Class I and Flat SED YSOs (green stars) and massive clumps (yellow diamonds) to a broken power law (Section 3.2) and obtain an estimate for the star forming threshold, Σ_{th} , of $129 \pm 14 M_{\odot} \text{ pc}^{-2}$ (grey shaded region). The slope changes from 4.6 below Σ_{th} to 1.1 above Σ_{th} .